Int J Earth Sci (Geol Rundsch) (2016) 105:1811–1830
DOI 10.1007/s00531-015-1276-x

ORIGINAL PAPER

Zircon dating and mineralogy of the Mokong Pan-African magmatic epidote-bearing granite (North Cameroon)

R. Tchameni[1,7] · F. Sun[2] · D. Dawaï[3] · G. Danra[1] · L. Tékoum[2] · E. Nomo Negue[1,4] · O. Vanderhaeghe[5] · C. Nzolang[6] · Nguihdama Dagwaï[6]

Received: 22 July 2015 / Accepted: 12 November 2015 / Published online: 8 December 2015
© Springer-Verlag Berlin Heidelberg 2015

Abstract We present the mineralogy and age of the magmatic epidote-bearing granite composing most of the Mokong pluton, in the Central Africa orogenic belt (North Cameroon). This pluton intrudes Neoproterozoic (~830 to 700 Ma) low- to high-grade schists and gneisses (Poli-Maroua group), and is crosscut or interleaved with bodies of biotite granite of various sizes. The pluton is weakly deformed in its interior, but solid-state deformation increases toward its margins marked by narrow mylonitic bands trending NNE–SSW. The magmatic epidote granitic rocks are classified as quartz monzodiorite, granodiorite, monzogranite, and syenogranite. They are medium- to coarse-grained and composed of K-feldspar + plagioclase + biotite + amphibole + epidote + magnetite + titanite + zircon + apatite. In these granites, the pistacite component [atomic $Fe^{+3}/(Fe^{3+} + Al)$] in epidote ranges from 16 to 29 %. High oxygen fugacity (log fO_2 − 14 to −11) and the preservation of epidote suggest that the magma was oxidized. Al-in hornblende barometry and hornblende–plagioclase thermometry indicate hornblende crystallization between 0.53 and 0.78 GPa at a temperature ranging from 633 to 779 °C. Zircon saturation thermometry gives temperature estimates ranging from 504 to 916 °C, the latter being obtained on samples containing inherited zircons. U/Pb geochronology by LA-ICP-MS on zircon grains characterized by magmatic zoning yields a concordia age of 668 ± 11 Ma (2σ). The Mokong granite is the only known occurrence magmatic epidote in Cameroon, and is an important milestone for the comparison of the Central Africa orogenic belt with the Brasiliano Fold Belt, where such granites are much more abundant.

Keywords Central Africa Pan-African orogenic belt · North Cameroon · Magmatic epidote-bearing granite

✉ R. Tchameni
rigotchameni@yahoo.fr

1 Department of Earth Sciences, Faculty of Science, University of Ngaoundéré, PO Box 454, Ngaoundéré, Cameroon

2 College of Earth Sciences, Jilin University, Changchun 130061, People's Republic of China

3 Department of Earth Sciences, Faculty of Science, University of Maroua, PO Box 814, Maroua, Cameroon

4 Department of Earth Sciences, Faculty of Science, University of Yaoundé I, PO Box 812, Yaoundé, Cameroon

5 GET, Observatoire Midi-Pyrénées, Université de Toulouse, CNRS, IRD, 31400 Toulouse Cedex, France

6 Department of Life and Earth Sciences, Higher Teachers' Training College, University of Maroua, PO Box 55, Maroua, Cameroon

7 Laboratoire GéoRessources, Université de Lorraine, 54506 Vandoeuvre-lès-Nancy Cedex, France

Introduction

The Late Neoproterozoic (Pan-African) Central African orogenic belt, north of the Congo Craton, was recognized in the early 1960s by the widespread occurrence of ~500–600 Ma Rb–Sr whole rock and mineral ages (Lasserre 1967). This orogenic belt straddles Cameroon, Chad, and Central Africa Republic, between the Congo Craton to the south and the western Nigerian Shield to the north (Fig. 1a, b). It corresponds to the southern part of the Saharan metacraton (Abdelsalam et al. 2002, 2011; Liégeois et al. 2013), and to the west continues into the Borborema Province of NE Brazil, where the shear zones control the emplacement of a large number of Brasiliano-Pan-African granitoids (Fig. 1a). It has long been recognized that

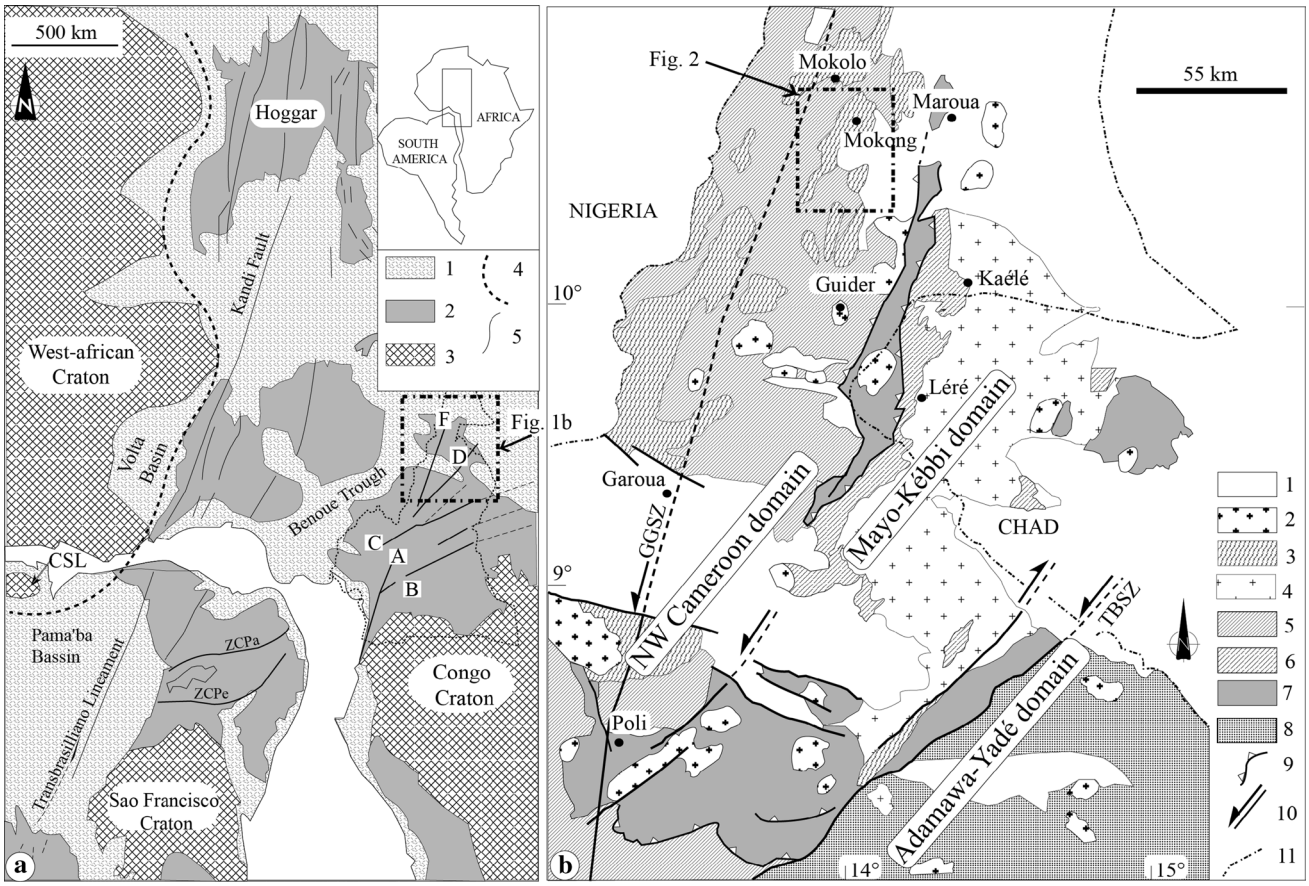

Fig. 1 **a** Pre-Mesozoic fit between the northern Borborema Province (NE Brazil) and Cameroon (after Caby 1989, modified): (*1*) Post-Brasiliano-Pan-African sediments; (*2*) Brasiliano-Pan-African belt; (*3*) Cratons; (*4*) Suture zone; (*5*) Shear zones: ZCPa: Patos; ZCPe: Pernambuco; *A*: Rocher du Loup shear zone; *B*: Sanaga fault; *C*: Central Cameroon shear zone; *D*: Tcholliré–Banyo shear zone; *E*: Godé Gormaya shear zone. **b** Geological sketch map of northern Cameroon (modified from Penaye et al. 2006 and Dawaï et al. 2013): (*1*) Post-Pan-African sediments; (*2*) Late to post-tectonic Pan-African granitoids; (*3*) syntectonic granite; (*4*) Mayo Kebbi batholith: tonalite, trondhjemite, and granodiorite; (*5*) medium- to high-grade gneisses of the NW Cameroon domain; (*6*) mafic to intermediate complex of the Mayo Kebbi domain (metadiorite and gabbro-diorite) and amphibolite; (*7*) Neoproterozoic low- to medium-grade volcano-sedimentary sequences of the Poli-Léré Group; (*8*) remobilized Paleoproterozoic Adamawa–Yadé domain; (*9*) thrust front; (*10*) strike slip fault: TBSZ = Tcholliré–Banyo shear zone; GGSZ = Godé-Gormaya shear zone; (*11*) state border

a strong geological correlation exists between NE Brazil and west-central Africa (e.g., Caby 1989; Castaing et al. 1994; Trompette 1997; Oliveira et al. 2006; De Witt et al. 2008; Van Schmus et al. 2008; Neves et al. 2012). In the Borborema Province, Late Neoproterozoic plutonism comprises several associations (Ferreira et al. 2004; Sial 1986; Sial et al. 2008; Brasilino et al. 2011), of which the high-K calc-alkalic rocks are the most voluminous (da Silva Filho et al. 1993; Ferreira et al. 2004, 2011; Ferreira and Sial 1997; Guimaraes et al. 2004; Sial et al. 2008). Magmatic epidote-bearing granitoids are widespread in northeastern Brazil, having been identified in five Neoproterozoic terranes: Seridó, Cachoeirinha-Salgueiro, Riacho do Pontal, Alto Pajeú, and the Macururé (Sial 1986, 1993; Galindo et al. 1995; Long et al. 2005). Experiments on epidote dissolution kinetics (Brandon et al. 1996) and on epidote stability in granitic melts (Schmidt and Thompson 1996) suggest that epidote textures offer a powerful means to estimate crystallization depth, pressure, and oxygen fugacity which are fundamental to characterize the conditions of pluton emplacement and growth and thus to understand the dynamics of crustal differentiation. In the Central Africa orogenic belt, the tectonic evolution involved voluminous granitic magmatism, like in the Borborema Province, but granite-bearing magmatic epidote has not been described so far. We present for the first time field observations, petrology, geochemistry, and zircon U/Pb geochronology of the magmatic epidote-bearing Mokong granitic facies, including analysis of epidote texture and mineral chemistry.

Geological setting

Northern Cameroon and southwestern Chad (Fig. 1b) are made of (1) Neoproterozoic (~830–700 Ma) low- to high-grade schists and gneisses of the Poli-Léré group that were deposited in a magmatic arc context, deformed and metamorphosed during the Pan-African (Toteu et al. 2006); (2) Pan-African pre-, syn-, and late-tectonic calc-alkaline granites emplaced between 660 and 580 Ma (Toteu et al. 2001; Penaye et al. 2006); (3) late- to post-tectonic alkaline granitoids (Penaye et al. 2006; Isseini et al. 2012) comprising basaltic and differentiated dykes followed by the formation of (4) several basins comprising unmetamorphosed sedimentary and volcanic rocks (Toteu et al. 2004; Van Schmus et al. 2008). Isotope dating indicates that most of the gneissic and granitic rocks of this domain are Neoproterozoic in age with minor Paleoproterozoic to Mesoproterozoic contribution (Isseini et al. 2012; Dawaï et al. 2013), contrasting with the abundant Paleoproterozoic ages that characterize the Adamawa–Yadé domain (Toteu et al. 2001; Penaye et al. 2004). This suggests that the NE–SW Tcholliré–Banyo shear zone, separating the Poli-Léré group from the Adamawa–Yadé domain, is a major boundary separating a juvenile Neoproterozoic upper crust on the western side, from older formations to the east (Toteu et al. 2001; Bouyo Houketchang et al. 2009; Isseini et al. 2012).

Structurally, two main deformation phases followed by late-orogenic shear zones are recorded in North Cameroon (Dumont et al. 1985; Nzenti et al. 1992; Toteu et al. 2004; Ngako et al. 2003, 2008). The first phase corresponds to a sub-horizontal foliation associated with isoclinal folds and N110°–140° stretching lineations, which are locally well preserved. The second phase is marked by vertical and NNE-trending foliations and by tight and upright folds. In the Poli area, syn-migmatitic N80°–N110° dextral and N160°–180° sinistral shear zones characterize this second phase. However, according to Ngako and Njonfang (2011), three major events characterize the formation of the Central African orogenic belt: The first one is ascribed to crustal thickening and ended at about 630–620 Ma; the second corresponds to left lateral movements (613–585 Ma); and the third event, characterized by right lateral wrench movements (585–540 Ma), has controlled the emplacement of post-collisional granitoids (Ngako et al. 2008; Kwékam et al. 2013).

The Mokong pluton

The Mokong pluton belongs to the NNE-trending suite of elongated syntectonic granitoids (Figs. 1b, 2) which intrude medium- to high-grade gneisses assigned to the Poli-Maroua group of the northwest Cameroon Pan-African domain (Toteu et al. 2006; Bouyo Houketchang et al. 2013). Most of the granitoids forming the Mokong pluton present a NE–SW- to NNE–SSW-trending magmatic foliation. The western and eastern boundaries of the Mokong pluton are strongly foliated, sheared, and mylonitized, with kinematic indicators of dextral movement. These mylonitic bands transposed the early N60 schistosity and N110°E sinistral shear zones. The pluton is mainly composed of two distinct granitic facies, namely magmatic epidote-bearing granite and biotite granite. In places, the Mokong pluton is overlain by Cenozoic volcanic formations and recent sediments.

The magmatic epidote-bearing granite (mEp granite)

The mEp granite is the main rock type of the Mokong pluton (Fig. 2). It intrudes the Neoproterozoic amphibolites and orthogneisses and contains xenoliths of these rocks. The pluton has an elliptical outcrop pattern (Fig. 2), and its NNE-trending long axis is more or less parallel to the regional tectonic fabric (NE–SW to NNE–SSW) of its country rocks. The pluton is weakly deformed in its interior, but solid-state deformation increases toward its margins where it is sheared (Fig. 3a, d). The major rock type is a porphyritic to equigranular medium- to coarse-grained granite with plagioclase and K-feldspar megacrysts up 3 cm long in random orientation in a medium-grained matrix (Fig. 3a, c, d). The internal foliation has steep dips (>40°) at the margins, becoming gentle or disappearing toward the core of the pluton where megacrystic feldspars are randomly distributed (Fig. 3c). This foliation, marked by subparallel tabular feldspars, biotite, and sometimes amphibole crystals, is roughly concordant with the pluton shape, consistent with a forceful expansion of the pluton. The foliation is also outlined by elongate 0.2 up to 5-m-long quartz monzodiorite enclaves (Fig. 3b). Many of these microgranular mafic enclaves have sharp contacts with the host granite, showing interfingered or rounded contours. The mEp granite is the focus of this study.

The biotite granite

This type consists of intrusions of various sizes (up to kilometer) crosscutting or interleaved with the mEp granite (Fig. 3d). Although both types of plutonic rocks are foliated, the biotite type contains xenoliths of the mEp type (Fig. 3e). Outcrops are exposed in the central and northwestern parts of the pluton (Fig. 2). The two sub-types can be distinguished: dominant pinkish biotite granite and gray biotite monzogranite, both characterized by fine- to medium-grained granular texture, and by the presence of biotite-rich enclaves, microgranular mafic magmatic enclaves, and schlieren. Dark green biotite is the most abundant mafic mineral (up to 10 vol%). It occurs as flakes filling interstitial spaces and forming

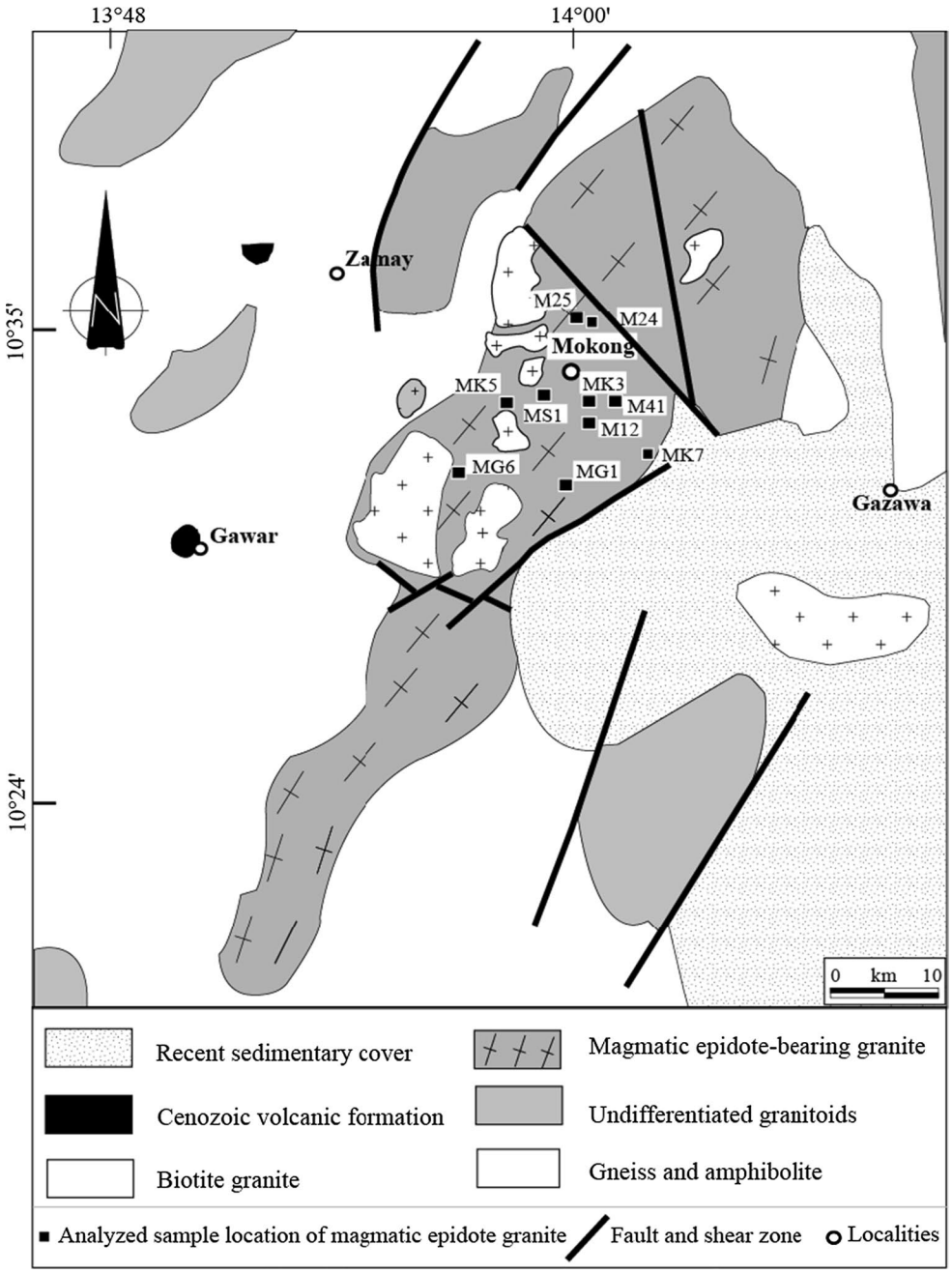

Fig. 2 Simplified geological *map* of the Mokong pluton, showing the locations of the analyzed samples in which magmatic epidote was recognized (*black squares*)

anhedral to subhedral glomerocrysts with large size variations (0.5–30 mm), is generally associated with feldspars, and marks the foliation. Plagioclase, K-feldspars (orthoclase and microcline), quartz, biotite, and accessory minerals (apatite, titanite, zircon, and oxides) are the dominant minerals. Titanite and oxides are abundant in the gray biotite sub-type.

Zircon U–Pb dating of mEp granite

Zircon grains from the magmatic epidote-bearing granite (sample MS-1) were separated using standard crushing, Wilfley table, magnetic separator, and heavy liquid separation. Zircon concentrates were cleaned using concentrated HF acid followed by H_2SO_4 acid and handpicked. Zircon grains were mounted as a single-crystal layer in epoxy disks and polished with 3- and 1-μm diamond spray to give a scratch-free surface. They were then imaged in cathodoluminescence (CL) using a Mono CL3 + (Gatan Company, England) at the State Key Laboratory of Continental Dynamics, Department of Geology, Northwest University, Xi'an (China). LA-ICP-MS dating was completed in the State Key Laboratory of Continental Dynamics in Xi'an. The laser ablation equipment was GeoLas200 M,

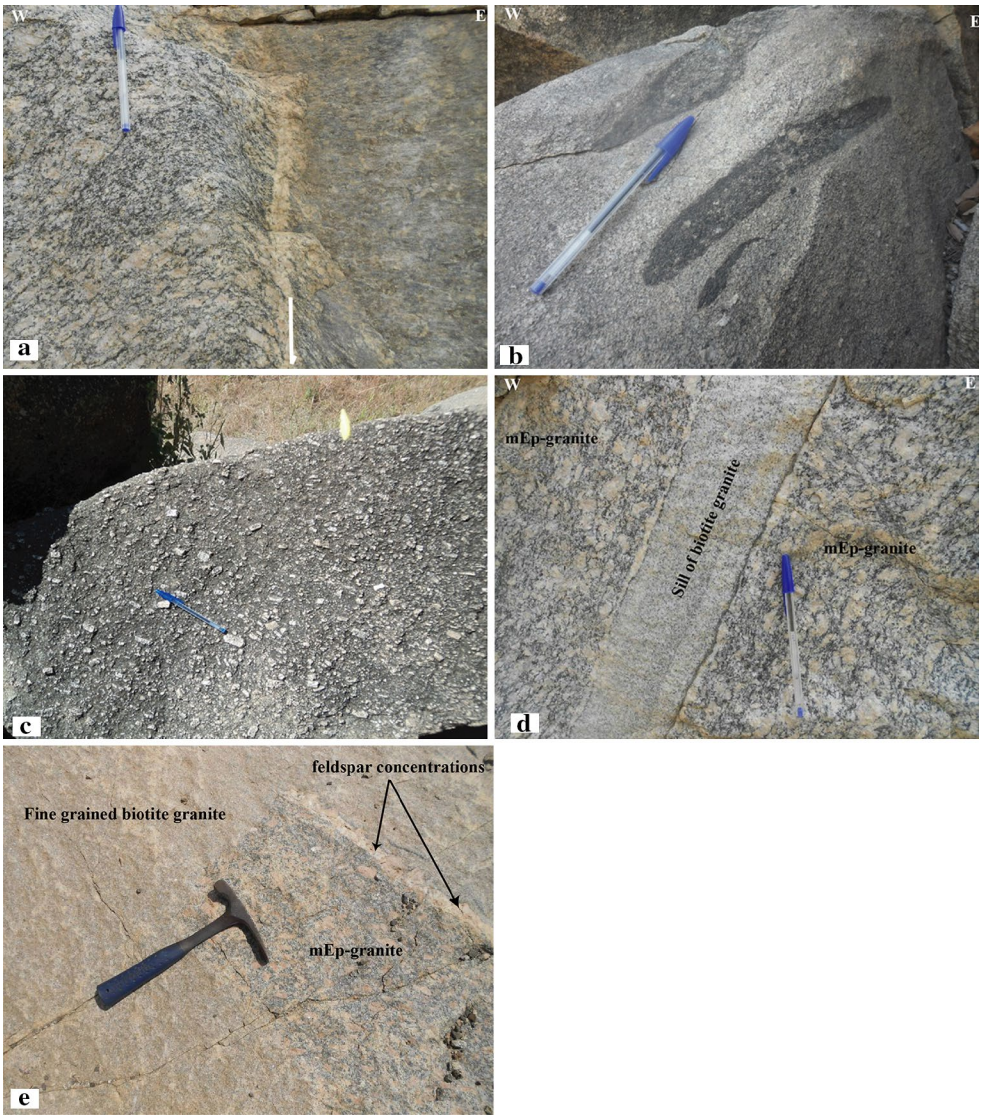

Fig. 3 Photographs field. **a** Eastern border of the Mokong mEp granite showing marks of the NNE–SSW magmatic foliation sheared dextrally. **b** Elongate quartz dioritic enclaves outline the magmatic foliation in Mokong mEp granite; **c** Core of the Mokong mEp granite showing irregular distribution of megacrystic feldspars; **d**, **e** the relationship between the mEp and the biotite granite types, indicating clearly point to their chronology

and inductively coupled plasma mass spectrometer was Agilent 7500a. During analysis, the synthetic glass NIST 610 was used to optimize the instruments. The standard zircon 91500 was used as an external standard to monitor the status of the machines and was analyzed twice before the analysis of the samples. Trace element concentrations were calibrated using 29Si as an internal standard for zircon and NIST SRM610 as an external standard. The detailed instrumental parameters and the protocol of analyses follow Yuan et al. (2004) and Liu et al. (2010). The raw data were then processed using the Glitter (version 4.0) program of Macquarie University, and the common lead was corrected following the method of Andersen (2003). The weighted mean age was calculated using Isoplot (version 3.23; Ludwig 2003). Analyses with >10 % discordance were excluded from the calculations. The isotopic ratios and age are quoted at 2σ, while the weighted mean is given at the 95 % confidence level. The LA-ICP-MS zircon U–Pb data analysis results and cathodoluminescence images are shown, respectively, in Table 1 and Fig. 4.

Most zircon crystals collected from sample MS-1 have euhedral, elongated shape with sharp facets and acute tips. Occasionally, the prisms are irregular, suggesting chemical corrosion or physical abrasion. The zircon crystals are mainly colorless and transparent, with lengths ranging from 150 to 300 μm and length-to-width ratios from 2.5:1 to

Table 1 LA-ICP-MS zircon U–Pb dating results of the Mokong magmatic epidote-bearing granite

Analysis	Pb	Th232	U238	Th/U	Pb207/Pb206		Pb207/U235		Pb206/U238		Pb207/Pb206		Pb207/U235		Pb206/U238		Pb208/Th232	
	ppm	ppm	ppm		Ratio	1σ	Ratio	1σ	Ratio	1σ	Age (Ma)	1σ	Age (Ma)	1σ	Age (Ma)	1σ	Age (Ma)	1σ
MS1-01	20.13	29.69	179.36	0.1655	0.06198	0.00234	0.93899	0.0419	0.10981	0.00423	673.3	78.72	672.4	21.94	671.6	24.55	698.7	30.53
MS1-02	26.36	21.68	245.18	0.0884	0.06209	0.00231	0.93995	0.04156	0.10971	0.00422	677.3	77.59	672.9	21.76	671.1	24.54	790.3	38.51
MS1-03	27.91	21.18	261.34	0.0810	0.0591	0.00213	0.89485	0.03882	0.10973	0.00422	570.9	76.68	649	20.8	671.2	24.51	650.3	31.85
MS1-04	74.80	57.92	735.33	0.0788	0.06215	0.00236	0.93929	0.04209	0.10954	0.00423	679.3	78.96	672.5	22.04	670.1	24.6	792.2	37.83
MS1-05	37.61	42.27	359.35	0.1176	0.06195	0.00267	0.93513	0.04599	0.10941	0.00427	672.3	89.73	670.3	24.13	669.3	24.81	652.3	36.62
MS1-06	45.71	31.73	437.72	0.0725	0.06194	0.00218	0.93638	0.04006	0.10959	0.00423	671.9	73.64	671	21.01	670.4	24.57	755.6	34.31
MS1-07	78.01	114.76	611.51	0.1877	0.06675	0.0028	0.99849	0.04813	0.10843	0.00424	830.0	85.11	703	24.45	663.6	24.67	1031.7	47.44
MS1-08	57.80	21.57	550.76	0.0392	0.06243	0.00212	0.94123	0.03933	0.10930	0.00422	688.7	70.68	673.5	20.57	668.7	24.51	1511.6	65.92
MS1-09	31.97	42.95	291.39	0.1474	0.06369	0.00472	0.95323	0.07307	0.10850	0.00458	731.4	149.55	679.8	37.99	664	26.66	1006.7	72.3
MS1-11	45.70	34.07	419.61	0.0812	0.06252	0.00471	0.94267	0.07348	0.10933	0.00465	691.8	152.98	674.3	38.41	668.8	27.01	639.9	62.46
MS1-12	41.94	31.67	408.75	0.0775	0.06036	0.00217	0.92005	0.04011	0.11052	0.00431	616.4	75.75	662.4	21.21	675.8	25.00	653.7	30.73
MS1-14	55.47	24.68	534.11	0.0462	0.06208	0.00261	0.93731	0.04554	0.10948	0.00432	676.8	87.46	671.5	23.87	669.8	25.1	804.8	52.08
MS1-15	35.75	29.13	373.43	0.0780	0.06275	0.00396	0.95209	0.06362	0.11002	0.00455	699.9	128.87	679.2	33.09	672.8	26.41	2025.5	157.72
MS1-16	36.81	37.85	355.92	0.1063	0.063	0.00235	0.95602	0.04281	0.11006	0.00432	708.1	77.29	681.2	22.22	673.1	25.08	749.1	33.77
MS1-17	41.86	50.3	403.06	0.1248	0.06126	0.00219	0.92936	0.04055	0.11003	0.00431	648.3	74.99	667.3	21.34	672.9	25.04	691.8	29.58
MS1-18	98.87	32.06	974.93	0.0329	0.06223	0.00202	0.94157	0.03872	0.10974	0.00429	681.9	67.85	673.7	20.25	671.3	24.89	668.3	30.41
MS1-21	32.34	24.32	306.81	0.0793	0.06195	0.00213	0.93592	0.04002	0.10960	0.00432	672.4	71.88	670.7	20.99	670.4	25.07	766.8	33.02
MS1-24	76.06	29.18	754.2	0.0387	0.06186	0.00305	0.92833	0.05105	0.10888	0.00441	669.3	102.12	666.8	26.88	666.2	25.66	1491	99.77

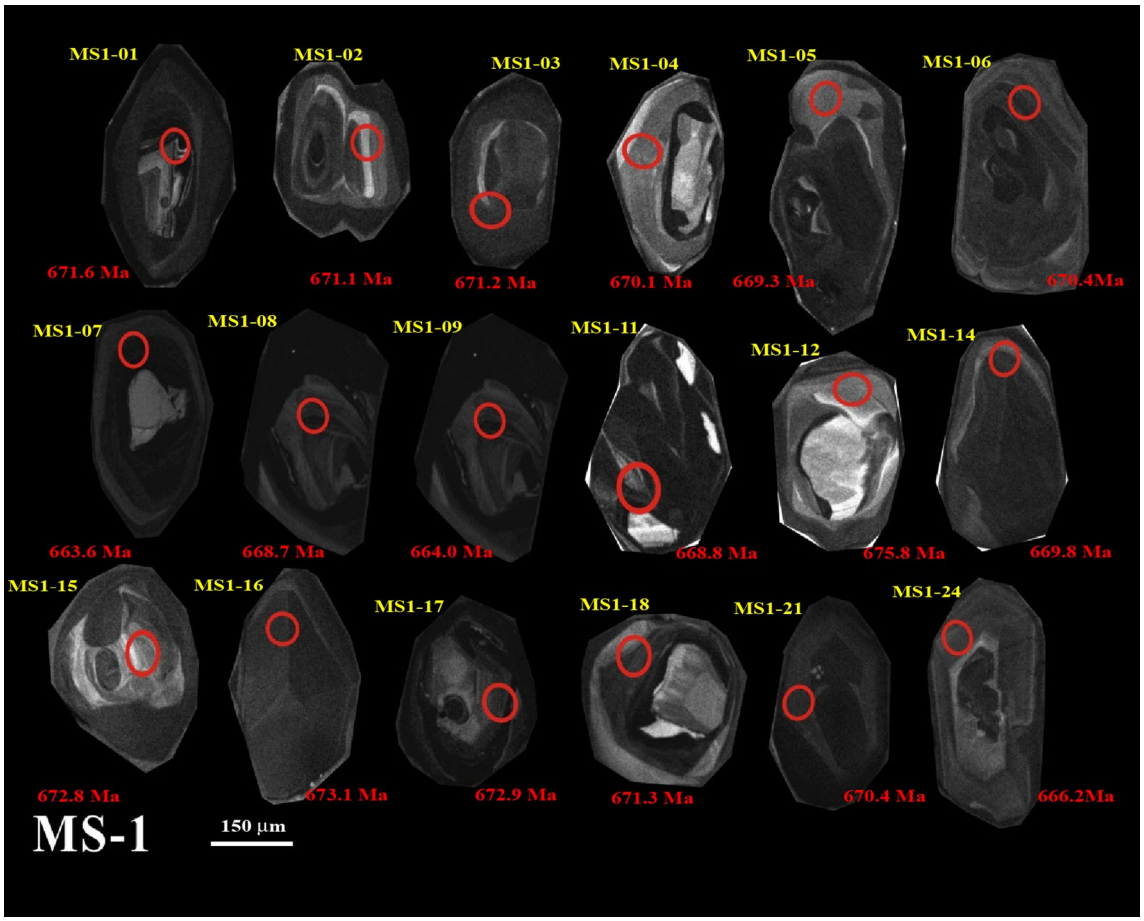

Fig. 4 Representative CL images of zircon grains from sample MS-1 showing $^{206}Pb/^{238}U$ ages

8:1. The CL investigation (Fig. 4) reveals that most crystals have oscillatory zoning. Some grains have irregular older or inherited cores, some being homogeneous and unzoned, whereas others exhibit oscillatory zoning; the core–rim boundary is often irregular and marked by a CL-bright thin band. The cores are small (5–40 μm), and only a few could be analyzed by LA-ICP-MS. To estimate the minimum age, eighteen analyses were carried out on the grains from MS-1 (Table 1), all of them being located on oscillatory-zoned rims. The analyses are concordant and yield a concordia age to 668 ± 11 Ma ($n = 18$; Fig. 5). This result is considered to be the crystallization age of the zircon and hence to be the emplacement age of the Mokong magmatic epidote granite.

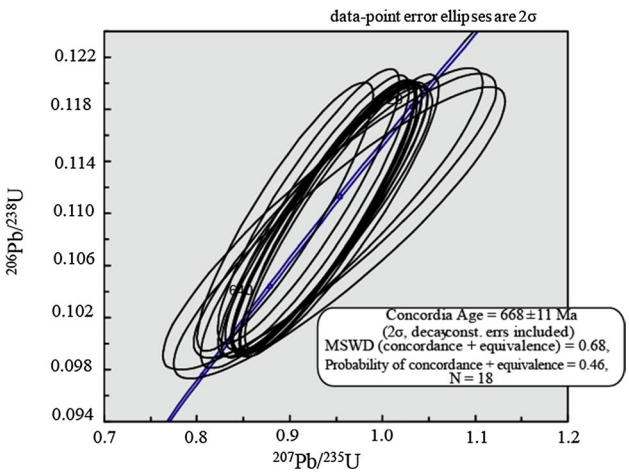

Fig. 5 U–Pb concordia plot and age determination for sample MS-1. The treatment of concordant age is after Ludwig (1998)

Petrography and mineral chemistry of the mEp granite

The Mokong epidote granite is mainly composed of K-feldspar, plagioclase, quartz, amphibole, biotite, epidote, and accessory phases (titanite, apatite, magnetite, and zircon) (Fig. 6). Secondary (alteration) products include epidote, chlorite, actinolitic amphibole, myrmekite, and sericite. Feldspars, amphibole, biotite, epidote, titanite, and

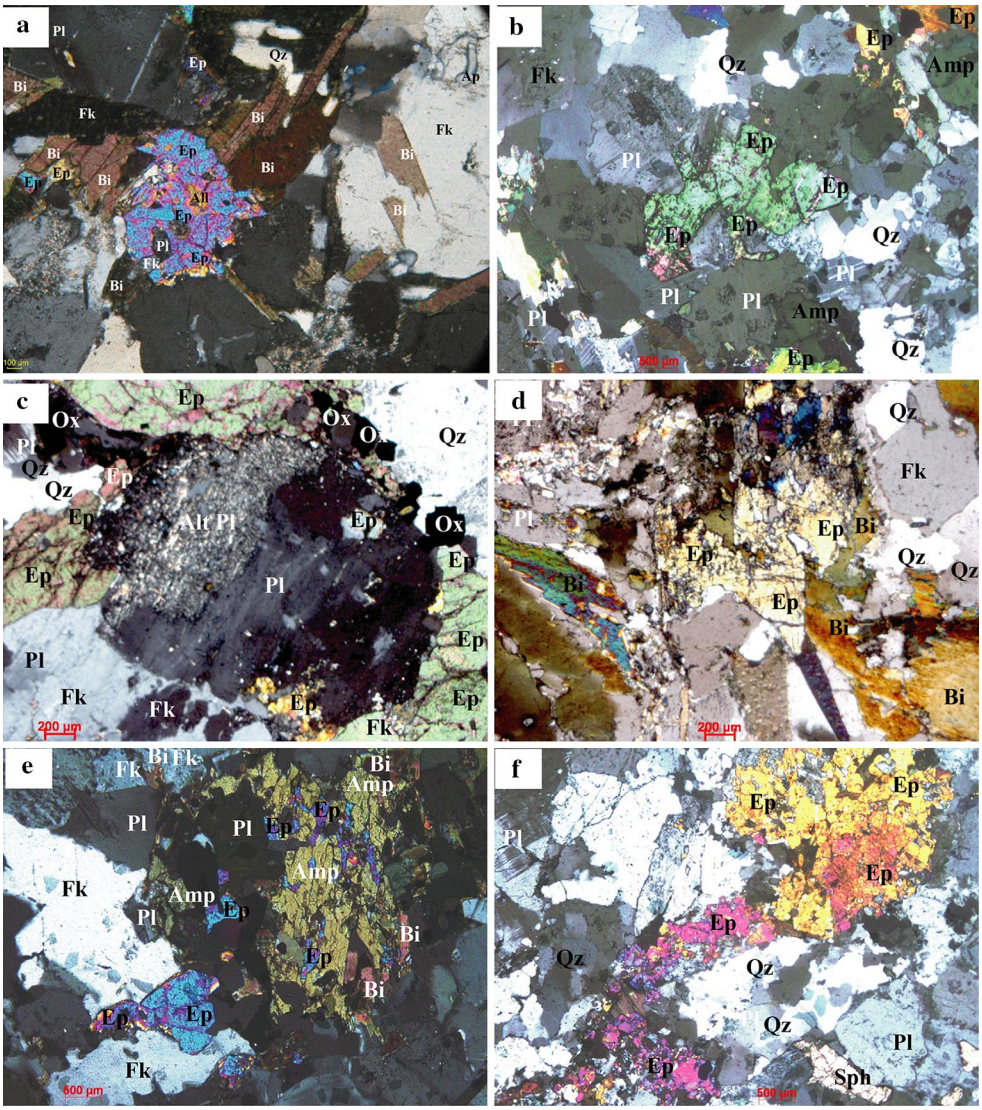

Fig. 6 Photomicrographs of various textural attributes of epidote: **a** euhedral magmatic epidote with minor inclusions of Fe oxide, plagioclase, and allanite; **b** and **c** late-crystallized magmatic epidote phases observed in intergranular spaces between plagioclase grains; **d** subhedral magmatic epidote showing resorbed margins; **d**, **e** secondary epidote phases formed at the expense of amphibole (**e**)

oxides were analyzed by electron microprobe at the GeoRessources laboratory (Université de Lorraine, Nancy). The operating conditions were maintained at 15 kv, 10 µA with beam exposure time of 6 s, applying ZAF correction. Chemical compositions and structural formulae are presented in Tables 2, 3, 4, 5, 6.

Feldspars

K-feldspar megacrysts (in porphyritic samples) are coarse perthitic microcline or orthoclase, typically displaying Carlsbad twinning, locally overprinted by cross-hatched twinning, suggesting incomplete orthoclase–microcline inversion. Their shape is subhedral, but under the microscope they display rounded corners and irregular edges rimmed by anhedral intergrowths of very fine-grained plagioclase, quartz, biotite, and myrmekite. Most megacrysts exhibit zoning and oriented inclusions of plagioclase near the core, in addition to inclusions of biotite and epidote. Microprobe analyses of K-feldspar (sample M41) indicate that the proportion of albite component in solid solution is in the range of 4–10 % (Table 2), and a composition ranging within Or_{89}–Or_{94}, with a gradual increase in albite toward the rim. Plagioclase grains (2–0.5 cm) are dominant in the groundmass. The larger grains commonly contain minor inclusions of hornblende and biotite. Some crystals show a weak zoning with slightly less sodic rim compositions, and with variable

Table 2 Feldspars selected microprobe analyses and structural formulae (on the basis of eight oxygens)

Sample	K-fs	M41			M21					MS1				M25			
Mineral		K-fs	K-fs	Pl2	Pl2	Pl2	K-fs	Pl	Pl	Pl	Pl	Pl	Pl	Pl	Pl	Pl	Pl
SiO_2	63.86	64.73	63.61	63.10	66.2	65.36	64.29	61.03	61.49	60.75	60.23	61.74	58.08	61.51	59.68	61.50	61.60
Al_2O_3	18.65	18.58	18.1	22.13	20.37	21.60	18.82	24.18	23.96	24.18	24.85	24.32	26.68	24.46	24.59	23.68	23.63
FeO	0.00	0.00	0.06	0.00	0.19	0.01	0.07	0.19	0.25	0.03	0.01	0.11	0.01	0.13	0.00	0.12	0.00
CaO	0.00	0.00	0.00	3.50	1.10	2.36	0.00	5.94	5.22	5.86	6.46	5.44	8.12	5.49	6.28	5.40	4.86
Na_2O	0.79	1.21	0.67	9.69	11.05	10.77	0.66	8.34	8.58	8.60	8.16	8.55	7.04	8.50	8.07	8.87	9.26
K_2O	16.00	15.38	15.89	0.11	0.06	0.09	16.05	0.11	0.17	0.1	0.17	0.08	0.05	0.21	0.1	0.16	0.09
Sum oxides	99.30	99.90	98.33	98.53	98.97	100.19	99.89	99.79	99.67	99.52	99.88	100.24	99.95	100.30	98.72	99.73	99.44
Si	2.976	2.988	2.990	2.827	2.933	2.872	2.975	2.720	2.738	2.716	2.687	2.732	2.596	2.723	2.690	2.741	2.749
Al	1.024	1.011	1.003	1.168	1.064	1.119	1.026	1.270	1.257	1.274	1.306	1.268	1.405	1.276	1.306	1.244	1.243
Fe	0.00	0.00	0.002	0.000	0.007	0.000	0.003	0.007	0.009	0.001	0.000	0.004	0.000	0.005	0.000	0.004	0.000
Ca	0.00	0.00	0.00	0.168	0.052	0.111	0.00	0.284	0.249	0.281	0.309	0.258	0.389	0.260	0.303	0.258	0.232
Na	0.071	0.108	0.061	0.842	0.949	0.918	0.059	0.721	0.741	0.745	0.706	0.734	0.610	0.730	0.705	0.767	0.801
K	0.951	0.906	0.953	0.006	0.003	0.005	0.948	0.006	0.010	0.006	0.010	0.004	0.003	0.012	0.006	0.009	0.005
Sum cation	5.022	5.013	5.009	5.011	5.008	5.025	5.011	5.008	5.005	5.023	5.018	5.001	5.003	5.006	5.009	5.024	5.031
%An	0.00	0.00	0.00	16.54	5.20	10.75	0.00	28.07	24.92	27.20	30.15	25.90	38.82	25.99	29.90	24.95	22.37
%Ab	6.98	10.68	6.02	82.84	94.46	88.76	5.88	71.31	74.12	72.24	68.91	73.65	60.90	72.82	69.53	74.17	77.13
%Or	93.02	89.32	93.98	0.62	0.34	0.49	94.12	0.62	0.97	0.55	0.94	0.45	0.28	1.184	0.57	0.88	0.49

Pl2 = secondary plagioclase

Table 3 Amphibole selected microprobe analyses and structural formulae calculated on the basis of 23 oxygens

Sample	M25							MS-1					
SiO_2	42.24	40.46	41.55	41.17	40.84	41.31	40.34	41.19	42.00	43.5	42.67	42.5	42.01
TiO_2	1.3	0.54	0.96	1.12	1.05	0.87	0.82	1.04	1.25	1.00	1.06	0.45	0.80
Al_2O_3	9.61	11.53	10.84	10.88	10.96	10.78	11.75	10.75	12.55	12.40	11.55	12.80	12.22
FeO	21.79	22.97	21.47	21.68	21.93	21.69	22.03	21.21	18.2	18.70	17.29	20.30	21.03
MnO	0.27	0.46	0.57	0.48	0.43	0.52	0.48	0.42	0.01	0.25	0.35	0.00	0.41
MgO	8.27	7.32	7.95	7.85	7.64	7.87	7.39	8.22	8.90	8.20	8.46	7.80	7.49
CaO	11.41	11.55	11.70	11.66	11.32	11.7	11.54	11.44	12.74	11.20	12.62	12.35	11.58
Na_2O	1.45	1.28	1.24	1.17	1.31	1.25	1.39	1.41	1.00	1.60	1.44	0.45	1.23
K_2O	1.37	1.44	1.38	1.44	1.50	1.43	1.54	1.43	1.45	1.60	1.71	1.4	1.75
Sum oxides	97.71	97.55	97.66	97.45	96.98	97.42	97.28	97.11	98.1	98.45	97.15	98.05	98.52
Si	6.436	6.187	6.318	6.284	6.270	6.319	6.180	6.298	6.332	6.503	6.561	6.385	6.342
Ti	0.149	0.062	0.110	0.129	0.121	0.100	0.094	0.120	0.142	0.112	0.123	0.051	0.091
Al	1.726	2.078	1.943	1.957	1.983	1.943	2.121	1.937	2.230	2.185	2.093	2.266	2.174
Fe^{2+}	2.685	2.977	2.756	2.776	2.827	2.732	2.830	2.782	2.135	2.229	1.618	2.486	2.517
Mn	0.035	0.059	0.073	0.062	0.056	0.067	0.062	0.054	0.001	0.032	0.045	0.000	0.052
Mg	1.878	1.669	1.802	1.787	1.748	1.795	1.688	1.874	2.000	1.827	1.939	1.747	1.686
Ca	1.862	1.892	1.906	1.907	1.862	1.918	1.893	1.874	2.058	1.794	2.079	1.988	1.873
Na	0.428	0.379	0.366	0.346	0.390	0.371	0.413	0.418	0.292	0.464	0.430	0.131	0.360
K	0.282	0.299	0.284	0.298	0.312	0.296	0.320	0.296	0.292	0.320	0.347	0.283	0.356
Sum cations	15.48	15.60	15.56	15.55	15.60	15.54	15.60	15.65	15.48	15.48	15.23	15.34	15.45
XMg	0.412	0.359	0.400	0.392	0.382	0.396	0.374	0.400	0.480	0.45	0.55	0.41	0.40
P (kbar)	5.30	6.96	6.31	6.37	6.52	6.29	7.18	6.29	7.56	7.01	6.42	7.79	7.43

Pressure estimated using the Al-in-hornblende barometry (Schmidt 1992)

Table 4 Biotite microprobe analyses and structural formulae (on the basis of 22 oxygens)

Sample	M25				MS					M41				
SiO_2	36.10	36.00	36.36	36.09	35.66	36.01	36.59	36.26	36.22	36.57	37.15	37.07	36.99	36.73
TiO_2	1.62	1.61	1.55	1.37	1.61	1.59	1.5	1.03	2.12	2.74	1.68	2.22	2.44	2.74
Al_2O_3	14.82	15.03	15.21	15.76	15.91	15.86	15.96	16.34	15.72	15.3	15.47	15.27	15.25	15.4
FeO	21.28	21.05	21.89	21.24	22.63	22.01	21.74	21.58	23.55	19.9	18.84	19.94	19.15	20.2
MnO	0.34	0.21	0.32	0.39	0.18	0.35	0.32	0.36	0.33	0.39	0.29	0.42	0.19	0.37
MgO	10.79	10.59	10.46	10.34	9.05	8.99	8.84	9.17	8.65	10.58	11.89	11.46	10.87	10.55
Na_2O	0.00	0.03	0.07	0.03	0.09	0.07	0.05	0.09	0.06	0.06	0.01	0.06	0.07	0.03
K_2O	9.85	9.87	9.38	9.79	9.92	9.84	9.50	9.49	9.67	10.08	10.1	9.98	9.91	10.1
Sum oxides	94.8	94.39	95.24	95.01	95.05	94.72	94.50	94.32	96.32	95.62	95.43	96.42	94.87	96.12
Si	5.617	5.618	5.622	5.596	5.570	5.621	5.686	5.648	5.589	5.605	5.658	5.621	5.674	5.603
Ti	0.189	0.189	0.180	0.160	0.189	0.187	0.175	0.121	0.246	0.316	0.192	0.253	0.281	0.314
Al^{IV}	2.383	2.381	2.378	2.404	2.431	2.380	2.314	2.352	2.410	2.395	2.342	2.379	2.326	2.396
Al^{VI}	0.334	0.383	0.394	0.476	0.498	0.539	0.608	0.648	0.449	0.369	0.434	0.350	0.431	0.372
Fe^{2+}	2.769	2.747	2.831	2.754	2.956	2.873	2.825	2.811	3.039	2.551	2.399	2.529	2.457	2.577
Mn	0.045	0.028	0.042	0.051	0.023	0.046	0.042	0.047	0.043	0.051	0.037	0.054	0.025	0.048
Mg	2.502	2.463	2.411	2.389	2.107	2.092	2.047	2.129	1.990	2.42	2.699	2.590	2.485	2.399
Na	0.000	0.009	0.021	0.009	0.027	0.021	0.015	0.027	0.018	0.018	0.003	0.018	0.021	0.009
K	1.955	1.964	1.850	1.936	1.976	1.960	1.883	1.886	1.904	1.971	1.962	1.930	1.940	1.965
Sum cations	15.79	15.78	15.73	15.78	15.78	15.72	15.60	15.67	15.69	15.69	15.73	15.72	15.64	15.68
XMg	0.475	0.473	0.460	0.464	0.416	0.421	0.420	0.431	0.396	0.486	0.529	0.506	0.503	0.482

degrees of saussuritization with formation of secondary epidote (Fig. 6c, f). Their compositions range between An_{17} and An_{39} (Table 2). The very fine-grained secondary plagioclase is made of albite (An_5) and more sodic oligoclase (An_{11}).

Amphibole

Amphibole occurs either as euhedral to subhedral crystals (0.2–5 mm), showing pale green to brownish green pleochroism, or pale green weakly pleochroic crystals forming cm to mm size, randomly distributed clots. Some twinned grains are also observed. Long axes of glomerocrysts are commonly aligned parallel to the foliation of the host rocks. Amphibole is more or less altered and contributed to the secondary epidote and actinolite crystallization (Fig. 6e). The analyses of amphibole (Table 3) classify them as calcic amphiboles according to the scheme of Leake et al. (1997), and more particularly as magnesio–hastingsite and hastingsite (Fig. 7a). The Mg/(Mg + Fe) ratio (0.40–0.64) is in accordance with the ranges prescribed for calc-alkalic granitoids (Mason 1985) and suggests crystallization of this phase under moderately high fO_2. The Si content varies from 6.1 to 6.5 atoms per formula unit (afu). Figure 7b illustrates a positive correlation between Al^{IV} and Al^{T} in the amphiboles, similar to that reported by Hammarstrom and Zen (1986).

Biotite

Dark green biotite is the most abundant mafic mineral, occurring as flakes filling interstitial spaces and as anhedral to subhedral glomerocrysts with large variation in size (0.5–30 mm) and generally aligned parallel to the foliation of the host rock. Apatite, epidote, titanite, and zircon are common inclusions in biotite. Secondary biotite crystals are included in amphibole (Fig. 6e) and alkali feldspar. Microprobe analyses of biotite (Table 4) indicate compositions lying approximately midway between phlogopite and annite (Fig. 7c). The range of molar Fe/(Fe + Mg) is 0.46–0.6. Biotite is poor in fluor (0.27–1.81 wt%). Its average FeO/MgO ratio varies from 1.5 to 2.7, consistent with the ranges reported from calc-alkalic granitoids by Abdel-Rahman (1994). In an MgO versus Al_2O_3 diagram (Fig. 7d), the biotite compositions plot in the calc-alkalic field. Their alumina saturation index (ASI, Al^{tot}/Ca + Na + K) is significantly low (average = 1.5) and reflects low alumina activity in the crystallizing magma (Zen 1988).

Epidote

Epidote occurs in several textural relationships in the mEp granites: (a) as euhedral to subhedral crystals with minor inclusions of Fe oxide, plagioclase, and allanite (Fig. 6a, c); some crystals are partially altered (Fig. 6d); (b) as a late-crystallized phase, observed in intergranular spaces

Table 5 Magmatic epidote selected microprobe analyses and structural formulae (cation calculated on the basis of 12.5 oxygens)

Sample	MS																
SiO_2	36.93	36.87	37.01	37.17	36.91	37.57	37.23	37.39	37.22	37.54	38	38.44	38.12	37.97	38.22	38.38	38,82
TiO_2	0.03	0.08	0.04	0.05	0.06	0.15	0.13	0.18	0.08	0.09	0.05	0.2	0.15	0.10	0.12	0.00	0.00
Al_2O_3	22.69	22.51	22.85	22.75	23.15	23.3	23.32	23.25	23.41	22.16	22.02	24.33	23.8	23.82	23.91	25.67	23.77
FeO	12.92	13.87	12.54	12.59	12.61	11.82	11.95	12	12.19	13.85	13.75	10.38	10.7	11.45	11.13	9.57	11.69
MgO	0.07	0.00	0.00	0.00	0.02	0.03	0.01	0.00	0.05	0.02	0.00	0.05	0.04	0.07	0.15	0.02	0.02
MnO	0.14	0.27	0.2	0.19	0.25	0.28	0.29	0.30	0.39	0.10	0.22	0.22	0.19	0.09	0.07	0.00	0.00
CaO	23.42	23.21	23.18	23.15	22.95	22.82	22.68	23.14	22.27	23.34	23.22	23.87	23.9	23.84	24.08	23.84	24,45
Sum oxides	96.20	96.81	95.82	95.9	95.95	95.97	95.61	96.26	95.61	97.1	97.26	97.49	96.9	97.34	97.68	97.48	98.75
Si	3.076	3.068	3.085	3.097	3.073	3.109	3.096	3.091	3.095	3.108	3.136	3.107	3.110	3.094	3.099	3.083	3.119
Ti	0.002	0.005	0.002	0.003	0.004	0.009	0.008	0.011	0.005	0.005	0.003	0.012	0.009	0.006	0.007	0.000	0.000
Al total	2.224	2.203	2.241	2.230	2.270	2.268	2.281	2.261	2.290	2.158	2.138	2.314	2.284	2.284	2.280	2.426	2.247
Mn	0.010	0.019	0.014	0.0134	0.017	0.019	0.020	0.021	0.027	0.007	0.015	0.015	0.013	0.006	0.005	0.000	0.000
Fe^{3+}	0.776	0.797	0.759	0.770	0.732	0.732	0.719	0.739	0.709	0.842	0.862	0.686	0.716	0.716	0.719	0.574	0.753
Fe^{2+}	0.120	0.165	0.112	0.104	0.143	0.083	0.109	0.088	0.135	0.114	0.084	0.013	0.012	0.061	0.032	0.067	0.030
Mg	0.009	0.000	0.000	0.000	0.002	0.004	0.001	0.000	0.006	0.002	0.000	0.006	0.005	0.008	0.018	0.002	0.002
Ca	2.090	2.069	2.070	2.067	2.047	2.023	2.021	2.050	1.984	2.070	2.053	2.067	2.089	2.081	2.092	2.052	2.105
Sum cations	8.30	8,32	8.29	8.28	8.29	8.25	8.26	8.26	8.25	8.31	8.29	8.22	8.24	8.26	8.25	8.20	8.26
%Ps	25.88	26.55	25.29	25.66	24.41	24.40	23.96	24.62	23.65	28.05	28.73	22.87	23.85	23.88	23.98	19.13	25.09

Sample	M25										M12		
SiO_2	38.92	37.49	38.15	38.11	38.34	37.73	38.29	37.63	37.08	36.91	38.35	38.47	38.23
TiO_2	0.00	0.13	0.09	0.02	0.11	0.01	0.12	0.04	000	0.03	0.12	0.14	0.200
Al_2O_3	25.02	25.01	23.26	24.2	23.99	24.3	24.97	22.81	22.94	22.84	24.73	26.4	26.68
FeO	11.22	11.76	12.98	12.23	11.43	11.56	10.55	12.77	12.14	12.72	10.49	8.55	8.45
MgO	0.14	0.00	0.00	0.00	0.01	0.00	0.09	0.03	0.00	0.01	0.12	0.03	0.03
MnO	0.00	0.00	0.47	0.25	0.34	0.00	0.00	0.26	0.26	0.57	0.04	0.18	0.12
CaO	24.17	23.45	22.42	23.47	23.19	23.27	23.53	22.98	23.41	22.36	23.66	23.71	23.32
Na_2O	0.00	0.00	0.00	0.01	0.00	0.04	0.03	0.00	0.01	0.00	0.03	0.00	0.01
K_2O	0.00	0.00	0.00	0.00	0.00	0.01	0.00	0.01	0.00	0.00	0.00	0.00	0.01
Sum oxides	99.47	97.84	97.37	98.29	97.41	96.87	97.55	96.52	95.83	95.44	97.51	97.48	97.03
Si	3.090	3.038	3.122	3.083	3.115	3.083	3.088	3.113	3.088	3.092	3.096	3.073	3.063
Ti	0.000	0.008	0.005	0.001	0.007	0.001	0.007	0.002	0.000	0.002	0.007	0.008	0.012
Al total	2.337	2.385	2.240	2.303	2.293	2.336	2.369	2.220	2.248	2.251	2.348	2.481	2.515
Mn	0.000	0.000	0.032	0.017	0.023	0.000	0.000	0.018	0.018	0.040	0.003	0.012	0.008
Fe^{3+}	0.663	0.615	0.760	0.697	0.707	0.664	0.631	0.780	0.752	0.749	0.651	0.519	0.485
Fe^{2+}	0.079	0.179	0.125	0.128	0.067	0.123	0.078	0.100	0.091	0.139	0.054	0.050	0.079
Mg	0.017	0.000	0.000	0.000	0.001	0.000	0.011	0.004	0.000	0.001	0.014	0.003	0.004
Ca	2.056	2.036	1.966	2.034	2.019	2.037	2.033	2.037	2.089	2.007	2.046	2.029	2.002
Sum cations	8.24	8.26	8.25	8.26	8.23	8.24	8.22	8.28	8.29	8.28	8.23	8.18	8.17
%Ps	22.10	20.51	25.34	23.23	23.57	22.13	21.03	26.00	25.07	24.97	21.72	17.29	16.18

between plagioclase, biotite, and amphibole (Fig. 6b); (c) as partly embayed subhedral grains within biotite and amphibole crystals (Fig. 6e); (d) as secondary texture crystals associated with quartz and albite (Fig. 6f). Textural criteria show that some epidote crystals are intergranular, suggesting that they grew at the end of magma crystallization in relation with oxidation by interaction with country rocks.

Several grains were selected, and 31 spots were analyzed (results reported in Table 5). Euhedral to subhedral crystals (13 spots) present high values (25–29 %) of pistacite [$Fe^{3+}/(Fe^{3+}+Al) \times 100$], well in the range specified by Tulloch (1979, 1986; Vyhnal et al. 1991) for typical magmatic epidote (Ps_{25}–Ps_{29}). Other grains that seem to be formed at the expenses of amphibole and plagioclase (Fig. 6e, f) have $Ps_{16–24}$, compatible with values of secondary epidote

Table 6 Titanite selected microprobe analyses and structural formulae (cation calculated on the basis of two oxygens)

sample	M25		M12		MK3		MS	
SiO_2	29.57	29.35	30.12	29.87	29.87	29.73	29.05	28.4
TiO_2	37.05	35.76	34.8	35.47	35.2	35.56	37.42	36.96
Al_2O_3	1.70	2.09	2.45	2.44	2.68	2.32	1.23	1.89
MnO	0.12	0.11	0.17	0.06	0.10	0.11	0.13	0.10
FeO	1.40	1.33	1.89	1.41	1.70	1.66	1.31	1.58
MgO	0.00	0.00	0.11	0.04	0.02	0.01	0.00	0.00
CaO	28.03	28.05	27.77	27.79	27.26	27.21	26.64	27.00
Sum oxides	97.87	96.69	97.31	97.08	96.83	96.60	95.78	95.93
Si	4.000	4.000	4.000	4.000	4.000	4.000	4.000	4.000
Ti	3.759	3.655	3.466	3.562	3.535	3.589	3.864	3.904
Al	0.270	0.335	0.383	0.384	0.422	0.367	0.199	0.313
Fe3+	0.000	0.010	0.151	0.053	0.042	0.044	0.000	0.000
Mn	0.013	0.013	0.019	0.007	0.011	0.012	0.015	0.012
Fe	0.158	0.141	0.058	0.104	0.147	0.142	0.151	0.186
Mg	0.000	0.000	0.022	0.008	0.004	0.002	0.000	0.000
Ca	4.062	4.096	3.951	3.987	3.911	3.922	3.930	4.074
Sum cations	12.26	12.25	12.05	12.11	12.08	12.07	12.16	12.49

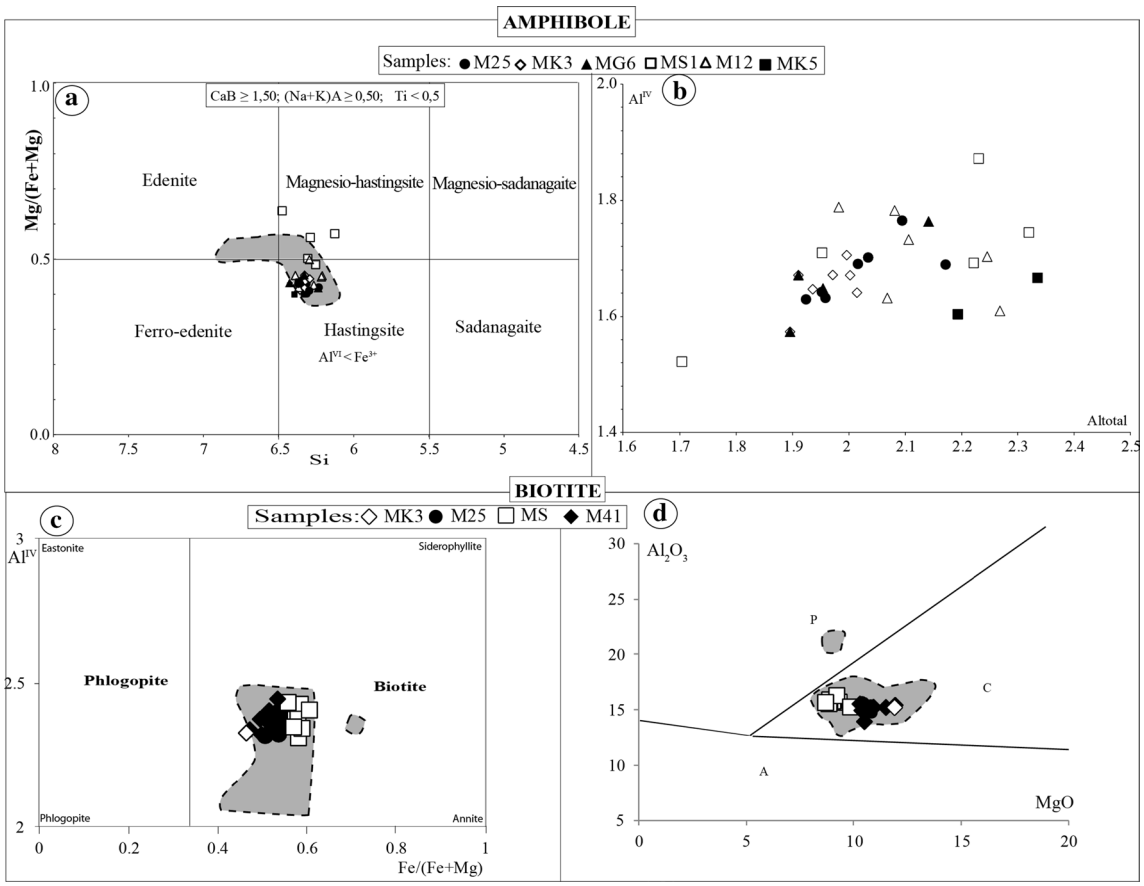

Fig. 7 **a** Classification of amphiboles from the studied samples (after Leake et al. 1997). **b** Relationship between Al^{IV} and Al^{T} in amphiboles. **c** Al_{tot} versus Fe/(Fe + Mg) diagram for biotite. **d** MgO versus Al_2O_3 diagram (after Abdel-Rahman 1994) showing biotite compositions plotting in the calc-alkalic field. A = alkalic, C = calc-alkalic, P = peraluminous. *Shaded fields* show amphibole and biotite analyses for epidote-bearing granites within the Alto Pajeú terrane, northeastern Brazil (Brasilino et al. 2011)

according the Tulloch´s criteria. Some examples from NE Brazil (Sial 1993; Sial et al. 2008; Ferreira et al. 2011), India (Rogers 1988), and Canada (Owen 1991; Farrow and Barr 1992) also lie in this range which is considered to be unequivocally mEp. The low TiO_2 contents (0.00–0.20 % with an average of 0.08 %) of all the analyzed epidote suggest that they are primary according to Evans and Vance (1987), who ascribe $TiO_2 < 0.2$ % to primary epidote.

Titanite and Fe oxides

Titanite is a common and abundant accessory phase in the mEp granites (about 2 % modal volume). It occurs as large euhedral crystals, up to 1 mm long as slightly pleochroic subhedral crystals, up to a few mm long, present in feldspar, along margins of hornblende and biotite crystals, or as euhedral grains in the groundmass, and as zoned and secondary fine-grained crystals associated with biotite. Titanite shows low Al content (0.16–0.42 afu, Table 6), suggesting high pressure of crystallization. According to Enami et al. (1993), titanite composition depends on pressure and temperature, high-temperature titanite having $Al + Fe^{3+}$ (afu) <1.4. In the mEp granites, the $Al + Fe^{3+}$ (afu) around 0.35 of titanite shows that this mineral was crystallized at high temperature, an observation supported by textural relationships which point to its early crystallization. Fe oxide minerals are rare, occurring as minute grains within or adjacent to biotite and titanite. All the analyzed Fe oxides correspond to pure magnetite.

Allanite was observed only in the sample S25 where it occurs as euhedral reddish brown prismatic zoned crystals. Many grains show metamictization that makes them more susceptible to alteration, which is commonly accompanied by hydration. The analyzed allanite crystals show high TiO_2 (0.81–2.51 %; Ti = 0.02–0.06 apfu) contents, with higher values in their core pointing to a formation in a compressive setting characterized by Ti < 0.2 apfu (Vlach and Gualda 2007).

Geochemical characteristics of the Mokong mEp granite

Whole-rock compositions from the representative samples of the Mokong mEp granite were determined using inductively coupled plasma atomic emission spectrometry (ICP-AES) for major elements, and inductively coupled plasma mass spectrometry (ICP-MS) for trace elements at CRPG-CNRS, Nancy (France). Sample preparation, analytical conditions, and limits of detection are detailed in Carignan et al. (2001). Table 7 lists representative whole-rock chemical analyses.

Nomenclature follows normative ANOR versus Q′ diagram (Fig. 8) of Streckeisen and Le Maitre (1979). The Mokong mEp granite evolves from quartz monzodiorite, granodiorite, monzogranite, and syenogranite fields. The porphyritic biotite–epidote sheared facies collected at the border of the pluton (sample MK7) plots in the quartz monzodiorite field. The granitoids are metaluminous to slightly peraluminous and belong to the I-type granitoids with A/CNK <1.12 (Shand 1927). The I-type geochemical signature of these granitoids is well supported by the mineralogy, more particularly the predominance of hornblende and biotite as mafic silicate minerals, and the abundance of titanite and magnetite as accessory phases. In the (Y + Nb) versus Rb discrimination diagram (Pearce et al. 1984, Fig. 9), the mEp granites plot within the volcanic-arc granite and syn-collisional granite fields.

The samples of mEp granite have an intermediate to acid composition (SiO_2 = 60.58–73.97 wt%) coupled with moderate Al_2O_3 (13.26–15.73 wt%) contents, high Mg values (Mg# = 35.4–63.5) and K_2O/Na_2O ratios (0.4–1.9, mostly >1). These rocks are enriched in Ba (508–1513 ppm) and have moderate to high Sr (205.3–1090 ppm), Rb (103.9–272.7 ppm). The Zr content ranges between 106.2 and 856.7 ppm, while Nb (4.80–13.39 ppm) and Y (3.89–29.33 ppm) are relatively low. The Rb/Sr ratios cluster around 0.19–1.05. The sheared biotite–epidote gray quartz monzodiorite sample MK7 is characterized by low Ba (186.8 ppm), high Nb (48.84 ppm), Y (79.07 ppm), Th (31.08 ppm), Sn (11.3 ppm), REE ($\sum$REE = 705 ppm), and Cu (102,2 ppm) contents. Chondrite-normalized REE patterns (Fig. 10) are moderately fractionated (La_N/Yb_N = 13.5–29.7). Except for sample MG46 which shows a weak positive Eu anomaly (Eu/Eu* = 1.1), no Eu anomalies (Eu/Eu* 0.5–0.9) are recorded.

The fine-grained mesocratic enclave (sample M24) plots in the quartz monzodiorite field in the normative ANOR versus Q′ diagram (Fig. 9). It is intermediate in SiO_2 composition (59.28 wt%) and shows high CaO (5.04 wt%), V (126.3 ppm), Zn (104.2 ppm), and Zr (238.9 ppm) contents and low Ba (489.9 ppm) content, compared to the mEp granites. Chondrite-normalized REE pattern (Fig. 10) is moderately fractionated (La_N/Yb_N = 5.06) with no Eu anomaly (Eu/Eu* 0.9). Major element trends and some trace element patterns such as positive correlations between Ba/Rb versus Zr/Rb, and Zr/Rb versus Sr/Rb point to fractional crystallization as an important petrogenetic process (Fig. 11). In these diagrams, the chemical composition of the Mokong mE granites is similar to the Conceição das Creoulas pluton located within the Alto Pajeú terrane at northeastern Brazil (Brasilino et al. 2011).

Table 7 Major (wt%) and trace (ppm) element compositions of the Mokong magmatic epidote-bearing granite

Rock types	Magmatic epidote-bearing granite									Enclave
Samples	M25	MK7	MK3	MG1	MS-1	M41	MK5	MG-6	M12	M24
Major elements (wt%)										
SiO_2	60.58	61.29	63.49	64.97	65.42	68.99	71.88	73.16	73.97	59.28
Al_2O_3	14.695	14.945	14.303	15.73	15.583	15.545	14.855	14.555	13.258	15.645
Fe_2O_3	7.328	6.991	5.995	4.673	4.89	2.798	1.468	1.441	1.394	7.634
MnO	0.0964	0.1373	0.0939	0.0876	0.0861	0.0424	0.0302	0.0225	0.0255	0.1304
MgO	2.225	2.005	1.643	2.36	2.525	0.809	0.386	0.407	0.217	2.666
CaO	4.576	3.799	3.321	3.636	3.312	2.381	1.703	1.947	1.089	5.036
Na_2O	3.027	4.65	3.662	3.846	4.101	4.028	4.048	4.05	2.956	3.639
K_2O	3.557	2.066	4.148	2.24	2.229	4.331	4.306	3.799	5.68	2.448
TiO_2	1.723	1.956	1.482	0.871	0.881	0.571	0.237	0.223	0.193	1.34
P_2O_5	0.6	0.78	0.75	0.28	0.27	0.16	0.1	0.06	0.05	0.39
PF	0.73	0.63	0.48	0.75	0.58	0.47	0.71	0.34	0.37	1.44
Total	99.14	99.25	99.36	99.45	99.86	100.12	99.72	100.01	99.2	99.64
Mg≠	50.00	50.18	51.17	63.21	63.53	53.68	48.96	50.70	35.37	50.97
Traces elements (ppm)										
Ba	1312	186.8	1512.8	948	802.4	949.9	807.1	767.2	507.6	489.9
Be	1.791	3.912	3.673	7.362	3.205	3.48	3.7	2.812	2.081	1.733
Cd	0.649	0.986	1.038	0.501	0.408	0.389	<L.D.	0.216	0.178	0.465
Co	16.52	11.62	11.6	11.18	11.72	4.705	2.322	2.21	1.519	17.86
Cr	22.44	27.2	24.55	75.23	81.04	15.35	8.011	4.912	<L.D.	19.6
Cs	0.977	4.107	6.467	7.668	4.659	2.646	3.331	1.708	2.375	2.32
Cu	28.08	102.2	20.66	7.426	<L.D.	17.47	10.58	14.96	7.023	34.11
Ga	23.49	29.65	27.27	24.89	23.4	23.46	21.58	19.09	18.28	21.23
Ge	1.414	1.68	1.745	1.514	1.439	1.169	1.056	0.975	0.931	1.299
Hf	14.39	20.13	19.2	7.212	6.947	8.485	4.052	3.349	4.439	6.061
Mo	1.947	1.096	1.643	0.516	<L.D.	0.83	<L.D.	0.566	0.874	1.862
Nb	8.47	48.84	8.22	13.39	11.01	10.85	6.528	4.798	5.984	9.916
Ni	14.55	13.59	12.6	17.96	23.22	6.079	<L.D.	<L.D.	<L.D.	15.7
Pb	18.50	17.69	28.89	26.91	17.93	33.19	26.33	25.74	32.36	9.803
Rb	103.9	201.9	272.7	153.3	179.4	175.5	190.2	143.4	215.5	61.34
Sc	11.6	11.63	8.99	9.27	9.73	4.49	3.1	2.23	2.1	17.37
Sn	3.615	11.3	7.906	6.713	5.772	3.459	1.292	1.379	1.401	3.103
Sr	535.2	332.8	1090	568.3	522.6	420.5	354.7	431.6	205.3	332.8
Ta	1.178	5.238	3.851	1.856	1.548	1.093	1.075	0.438	0.479	0.863
Th	9.526	31.08	29.1	12.86	9.638	18.89	15.48	7.719	42.21	4.807
U	1.908	8.019	7.409	2.376	4.024	3.124	2.416	1.721	5.157	1.646
V	138.5	97.2	79.03	77.83	80.35	39.45	17.81	16.73	11.08	126.3
Y	29.33	79.07	38.52	22.79	21.79	20.58	7.35	3.881	8.93	32.38
Zn	148.9	174	151.7	105.9	131.5	77.64	41.15	48.3	41.37	104.2
Zr	612.1	856.7	823.9	268.7	257.3	347	138.8	106.2	150.7	238.9
REE										
La	64	138.1	108.2	42.66	37.56	60.2	26.8	18.91	32.24	21.93
Ce	142.1	298.5	226.4	88.85	76.6	127.6	54.59	35.91	64.98	47.29
Pr	17.67	37.3	27.5	10.78	10.46	14.73	5.553	3.905	6.295	6.093
Nd	69.96	143	102.8	40.9	40.63	55.24	18.52	13.28	20.08	25.94
Sm	14.03	28.11	17.14	7.805	7.74	10.75	2.689	1.994	3.32	6.219
Eu	3.01	4.044	2.869	1.667	1.561	1.648	0.598	0.547	0.622	1.826
Gd	10.27	19.88	11.38	5.74	5.519	7.427	1.632	1.25	2.346	5.748

Table 7 continued

Rock types	Magmatic epidote-bearing granite									Enclave
Samples	M25	MK7	MK3	MG1	MS-1	M41	MK5	MG-6	M12	M24
Tb	1.383	2.77	1.469	0.791	0.773	0.963	0.193	0.137	0.317	0.918
Dy	6.85	14.89	7.446	4.336	4.221	4.952	1.043	0.69	1.707	5.794
Ho	1.157	2.75	1.309	0.817	0.794	0.821	0.222	0.129	0.338	1.208
Er	2.59	7.119	3.383	2.096	2.097	1.933	0.702	0.394	0.853	3.18
Tm	0.314	0.994	0.464	0.296	0.297	0.241	0.121	0.061	0.121	0.469
Yb	1.897	6.496	3.286	1.985	1.999	1.481	0.908	0.457	0.829	3.111
Lu	0.258	0.875	0.539	0.294	0.295	0.208	0.152	0.077	0.135	0.485
LaN/YbN	24.20	15.25	23.62	15.42	13.48	29.16	21.17	29.68	27.89	5.056
∑REE	335.49	704.83	514.18	209.02	190.55	288.19	113.72	77.74	134.18	130.21
Eu*/Eu	0.77	0.52	0.63	0.76	0.73	0.56	0.87	1.06	0.68	0.93
T °C Zr (HW)	702	611	916	504	844	608	718	765	663	
T °C P_2O_5 (HW)	1139	1096	1090	1040	949	976	926	877	770	
T °C (B & H)	779		752	756	643		750	633	650	

Zr T °C (zircon saturation temperature in the Mokong granitoids) = −273 + 12.900/17.18–ln(Zr) (Watson 1987)

T °C (B & H): Solidification temperature calculated from equations of Blundy and Holland (1990) and Holland and Blundy (1994)

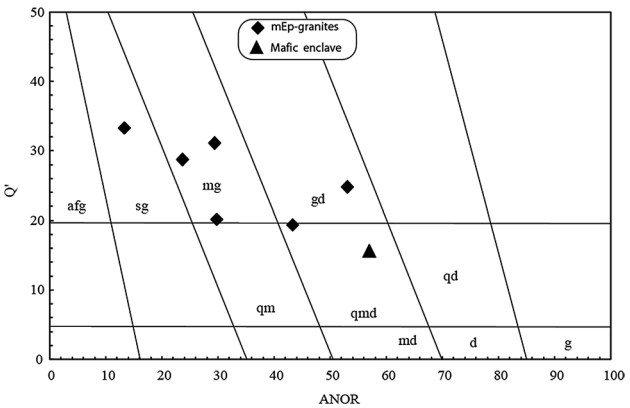

Fig. 8 Streckeisen and Le Maitre (1979) ANOR-Q′ normative diagram. Q′ = 1000/(Q + Or + Ab + An), ANOR = 100An/(An + Or). afg, alkali feldspar granite; *sg* syenogranite, *mg* monzogranite, *gd* granodiorite, *qm* quartz monzonite, *qmd* quartz monzodiorite, *qd* quartz diorite, *md* monzodiorite, *d* diorite, *g* gabbro

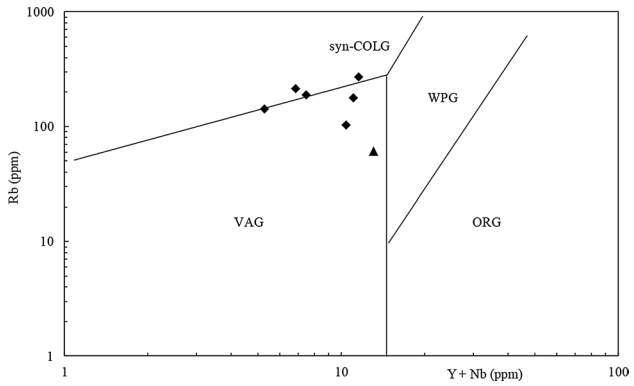

Fig. 9 Rb versus Yb + Nb tectonic discrimination diagrams of Pearce et al. (1984) for the granitoids and related dioritic enclave. *Symbols* as in Fig. 8

Estimation of physical parameters of emplacement

Al-in-hornblende barometry

The linear variation in Al content in amphibole of calc-alkalic granitoids with crystallization pressure/depth has been used in geobarometric estimates (Schmidt 1992). The empirical barometric equation proposed by Hammarstrom and Zen (1983, 1986) has been subjected to refinement and further calibration to increase the precision level to 1 kbar (Hollister et al. 1987; Johnson and Rutherford, 1989). Schmidt (1992) experimentally calibrated the field-based barometric equation of Hammarstrom and Zen (1986), expanding its applicability up to the 1.3 GPa pressure level, and maximum Alt up to 3.37 afu and have used it for H_2O saturated melts. According to Anderson and Smith (1995) and Anderson (1996), temperature, fO_2, and total pressure influence mafic silicate mineral chemistry, but fO_2 is the main controlling factor. They demonstrated that this barometer yields a falsely elevated pressure when applied to low-fO_2 plutons with iron-rich hornblende, even if hornblende is accompanied by the full barometer assemblage. With increasing fO_2, the Fe/(Fe + Mg) ratio for hornblende and biotite

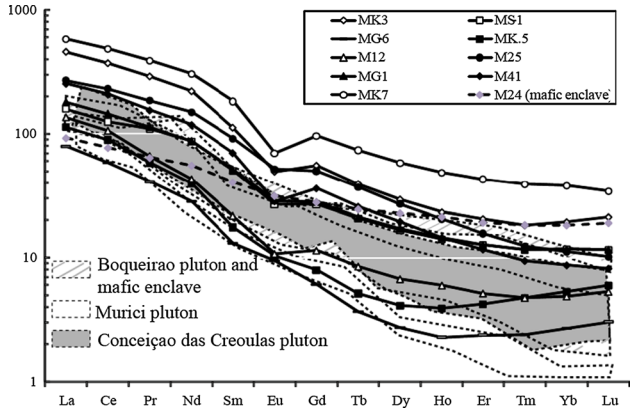

Fig. 10 Chondritic-normalized REE patterns for the Mokong mEp granites and its enclaves normalizing values from Sun and McDonough (1989). The *shaded fields* correspond to three epidote-bearing granites within the Alto Pajeú terrane, northeastern Brazil (Brasilino et al. 2011)

markedly decreases, independent of the whole-rock Fe/Mg ratio.

Given these considerations, we have applied this barometry to the samples characterized by the mineral assemblage including quartz, ferromagnesian silicates, euhedral titanite, and magnetite, and Fe/(Fe + Mg) in hornblende in the 0.40–0.65 range. The pressure of crystallization of the magma (Table 5) was calculated according to the following equation (Schmidt 1992): P (±0.6 kb) = −3.01 + 4.76Al_{tot}. The calculated pressures range between 5.3 and 7.8 kbar (average is 6.6 kb) for the Mokong magmatic epidote granites.

Hornblende–plagioclase, Zr, and P thermometry

Solidification temperatures were calculated from the semiempirical thermometer of Blundy and Holland (1990) and Holland and Blundy (1994), applied to chemical analyses of coexisting plagioclase and amphibole. The calculation is pressure-dependent; we adopted pressures calculated from Schmidt's (1992) Al-in-hornblende barometer. Beyond this, the compositions of amphibole and plagioclase fit all of Holland and Blundy's applicability criteria. This is valid for a temperature range of 500–1000 °C for plagioclase with <7.8 Si afu. The level of uncertainty in these calculations was subsequently reduced from ±75 to ±35 °C (Holland and Blundy 1994). The calculated crystallization temperatures for the studied magmatic epidote-bearing granites lie between 633 and 779 °C (Table 7).

Whole-rock Zr abundances can also be used to estimate temperatures in Zr-saturated granitic melts (Watson 1987). Watson and Harrison (1984) showed experimentally that zircon solubility is negatively correlated with SiO_2 (Fig. 12a). This method assumes that the zircon is not inherited from the source and does not represent a cumulate phase, and is based on the fact that zircon is usually the first mineral to crystallize. The CL investigation (Fig. 4) reveals that some zircon crystals have irregular and inherited cores, suggesting all zircons from the source have not been dissolved. This indicates that saturation has been reached during the genesis of magma or before the emplacement of the rocks. Zr thermometry obtained from Watson's (1987) zircon saturation equation [T (°C) = −273 + 12.900/17.18 − ln(Zr)] is 504–916 °C for the Mokong mEp granites with

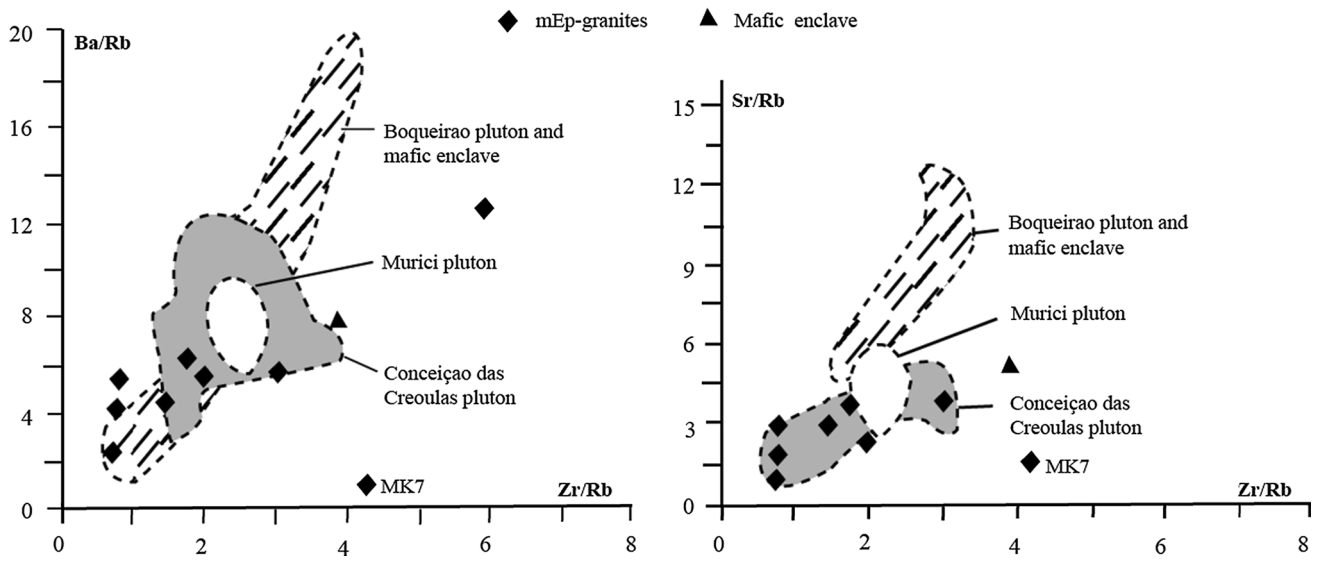

Fig. 11 Ba/Rb versus Zr/Rb, and Zr/Rb versus Sr/Rb diagrams, for the magmatic epidote granites and mafic enclave. The *shaded fields* are the same as in Fig. 10

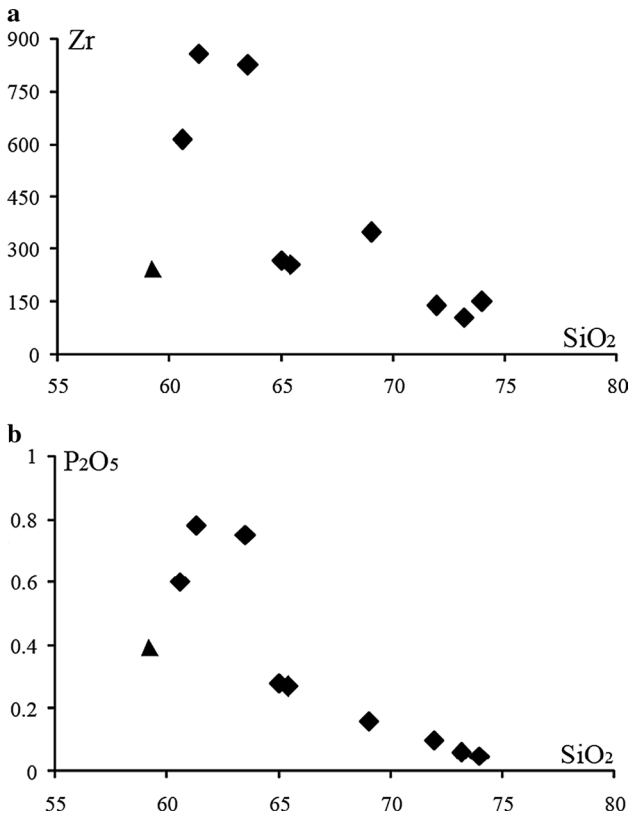

Fig. 12 Whole-rock Zr versus SiO_2 (**a**) and P_2O_5 versus SiO_2 (**b**) *plots* for representative samples of the studied rocks. *Symbols* are the same as in Fig. 11

average at 703 °C (Table 7). The highest value is obtained from the sample MK3 which contains large crystals of zircon; the value of 844 °C comes from sample MS-1 which contains inherited zircon cores (Fig. 4). This suggests that these high values have no physical meaning. The lower values obtained from sample MG1 yield the zircon saturation temperatures between 608 and 765 °C.

Watson (1987) quantified the conditions under which apatite can precipitate in common magma types, and has shown that temperature and silica content of the magma are critical in determining the P_2O_5 content in the magma required for apatite to crystallize. Green and Watson (1982) experimentally demonstrated a close, pressure-independent relationship between apatite saturation and SiO_2 concentration in the melt, establishing P_2O_5 abundance as a function of silica content at which apatite starts crystallizing (Fig. 12b). This correlation can be applied as a tool to estimate the minimum liquidus temperature using the whole-rock P_2O_5 and SiO_2 contents. These experiments were performed in hydrous high-K calc-alkalic rocks, which make them applicable to estimate the minimum liquidus temperatures for these granites. Data from this thermometer yield temperatures between 770 and 1139 °C, much higher than those from the zircon saturation method (Table 7).

Oxygen fugacity $f(O_2)$ estimate

Since oxygen fugacity of the magma is closely governed by its source material, it is difficult to use the end product to establish the oxygen fugacity of primary magmas. According to Enami et al. (1993), some inferences can be made using the rock mineral assemblage and mineral chemistry. The presence of Mg-rich amphiboles (Fe/(Fe + Mg) = 0.40–0.65 in our mEp granite) of early biotites, euhedral titanites, and magnetite in felsic rocks indicates that the host magma was relatively oxidized (Anderson and Smith 1995). Pistacite ($Ps_{25–29}$) is compatible with crystallization at higher oxygen fugacities. Wones (1989) demonstrated that the titanite + magnetite + quartz assemblage in granitic rocks allows an estimate of relative oxygen fugacity as follows: $\log f(O_2) = -30930 + 14.98 + 0.142(P - 1)/T$, where T is in Kelvin and P in bar. We adopted average pressures calculated from Schmidt's (1992) Al-in-hornblende barometer for each sample. Accordingly, the above equation yields the log oxygen fugacity range between −11 and −14 for the Mokong magmatic epidote granites.

Discussion

This preliminary study shows that the Mokong magmatic epidote-bearing granitoids intruded amphibolites and orthogneisses basement and contain xenoliths of these rocks. They are crosscut or interleaved with biotite granitoids as dykes or massifs and characterized by the presence of early crystallizing epidote, amphibole, biotite, euhedral titanite, and magnetite, indicating that the magma was relatively oxidized. Epidote exhibits both magmatic (Ps_{25}–Ps_{29}) and secondary (Ps_{16}–Ps_{24}) textures. This compositional variation in epidote (25–29 % Ps) is consistent with values proposed by Johnston and Wyllie (1988), and by Tulloch (1979) for magmatic epidote. Other grains that seem to be formed at the expense of plagioclase and amphibole have $Ps_{16–24}$, compatible with values of secondary epidote according to the Tulloch´s criteria (1979, 1986). Naney (1983) showed that epidote is stable in synthetic H_2O-saturated tonalitic and granodioritic melts at $f(O_2)$ values between the nickel–bunsenite (NB) and magnetite–hematite (MH) buffers, at temperatures between the solidus (600 °C) and approximately 700 °C, and at pressures at least in the 600–800 MPa range. Zen and Hammarstrom (1984) proposed that magmatic epidote crystallizes near the solidus of the crystallizing magma according to the following schematic reaction: 2 hornblende + alkali

feldspar + 1 magnetite + nH_2O + mO_2 = 3 epidote + 3 biotite + 6 quartz.

The aluminum-in-hornblende barometer and hornblende–plagioclase thermometer indicate that the emplacement of the Mokong mEp granite took place within a pressure interval 500–800 MPa (20–25 km), and based on plagioclase–hornblende pairs, we estimate a solidus temperature between 633 and 779 °C. The presence of magmatic epidote in various textural relationships suggests a large temperature range of crystallization, above its stability field of ~600 MPa (Schmidt and Thompson 1996), with subsequent rapid transport upward. Alternatively, the stability field of magmatic epidote could have extended to shallower crustal levels if fO_2 had been sufficiently high (Holdaway 1972). A log oxygen fugacity between −11 and −14 and values of Fe/(Fe + Mg) in amphibole from 0.40 to 0.65 indicate that oxidizing conditions prevailed the Mokong magmatic epidote granite.

The U–Pb zircon concordant age of 668 ± 11 Ma (2σ) obtained from for the Mokong mEp granite is slightly higher than the other ages obtained from the syn-tectonic granitoids of North Cameroon (660–580 Ma; Toteu et al. 2004; Dawaï et al. 2013) and NE Brazil (650–620 Ma; Sial et al. 1999, 2008; Ferreira et al. 2004), but agrees with previous ages obtained from the deformed tonalite at Gauthiot falls (664 ± 5.1 Ma; Penaye et al. 2006) in southwest Chad (Mayo Kebbi domain) and with the Kaélé deformed granite (677 ± 40 Ma; Lasserre 1967), the northern extension of the Mayo Kebbi batholith in Cameroon (Fig. 1b). In northeastern Brazil, magmatic epidote is more abundant and better preserved in the older group of plutons (650–630 Ma) in the Transversal Zone (Brasilino et al. 2011; Ferreira et al. 2011).

Conclusions

The Mokong pluton belongs to the NNE-trending suite of elongated syntectonic granitoids which intrude low- to high-grade schists and gneisses assigned to the Poli-Maroua group of the northwest Cameroon Pan-African domain. This pluton consists of two main units: a magmatic epidote-bearing granite and a biotite granite. The magmatic epidote-bearing granite derives from high-K calc-alkaline, I-type magma emplaced under oxidizing conditions at 668 ± 11 Ma. Textures and the compositional variation in many epidote grains (25–29 % Ps) suggest a magmatic origin. Nevertheless, some other grains (16–24 % Ps) appear as secondary and formed at the expense of plagioclase and amphibole. The aluminum-in-hornblende barometer and hornblende–plagioclase thermometer indicate an emplacement pressure interval of 5–8 kbar (20–25 km) for the Mokong magmatic epidote-bearing granite and a solidus temperature between 633 and 779 °C. This discovery of an epidote-bearing granite strengthens the correlation between the NNE-trending shear zone of the Central African orogenic belt and its continuation in the Borborema Province of NE Brazil but. Further studies are needed to know whether the Mokong mEp granite is a unique occurrence in Cameroon, or whether it represents part of a larger system similar to what is known in Brazil.

Acknowledgments This study was performed during a Senior Research Fellowship of Tchameni Rigobert (RT) at "Laboratoire Géoressources de l'Université de Lorraine, France," funded by AUF (Agence universitaire de la Francophonie) under the Project No. 51011SU201. RT is grateful to Pr Jacques Pironon for his supervision. The authors are thankful to Pierre Barbey whose comments and suggestions have helped improve the original manuscript and Olivier Rouer for his assistance during the electron microprobe analyses. We are also grateful to Valderez Ferreira and Jean Luc Bouchez for comments and suggestions made on an earlier version of this paper.

References

Abdel-Rahman AFM (1994) Nature of biotites from alkaline, calc-alkalic, and peraluminous magmas. J Petrol 35:525–541

Abdelsalam MG, Liégeois JP, Stern RJ (2002) The Saharan metacraton. J Afr Earth Sci 34:119–136

Abdelsalam MG, Gao SS, Liégeois JP (2011) Upper mantle structure of the Saharan metacraton. J Afr Earth Sci 60:328–336

Andersen T (2003) Correction of common lead in U–Pb analyses that do not report ^{204}Pb. Chem Geol 192:59–79

Anderson JL (1996) Status of thermobarometry in granitic batholiths. Trans R Soc Edinb Earth Sci 87:125–138

Anderson JL, Smith DR (1995) The effects of temperature and fO_2 on the Al-in-hornblende barometer. Am Mineral 80:549–559

Blundy JD, Holland TJB (1990) Calcic amphibole equilibria and a new amphibole—plagioclase geothermometer. Contrib Mineral Petrol 104:208–224

Bouyo Houketchang M, Toteu SF, Deloule E, Penaye J, Van Schmus WR (2009) U–Pb and Sm–Nd dating of high-pressure granulites from Tcholliré and Banyo regions: evidence for a Pan-African granulite facies metamorphism in north-central Cameroon. J Afr Earth Sci 54:144–154

Bouyo Houketcham M, Penaye P, Barbey P, Toteu SF, Wandji P (2013) Petrology of high-pressure granulite facies metapelites and metabasites from Tcholliré and Banyo regions: geodynamic implication for the Central African Fold Belt (CAFB) of north-central Cameroon. Precambrian Res 224:412–433

Brandon AD, Creaser RA, Chacko T (1996) Constraints on rates of granitic magma transport from epidote dissolution kinetics. Science 271:1845–1848

Brasilino RG, Sial AN, Ferreira VP, Pimentel MM (2011) Bulk rock and mineral chemistries and ascent rates of high-K calc-alkalic epidote-bearing magmas, Northeastern Brazil. Lithos 127:441–454

Caby R (1989) Precambrian terranes of Benin-Nigeria and northeast Brazil and the Late Proterozoic South Atlantic fit. Geol Soc Am Spec Pap 230:145–150

Carignan J, Hold P, Mevelle G, Morel J, Yeghichevan D (2001) Routine analysis of trace elements in geological samples using flow injection and low pressure on line liquid chromatography coupled to ICP-MS: a study of geochemical reference materials BR, DRN, UB-N, AN-G and GH. Geostand Newsl 25:187–198

Castaing C, Feybesse JL, Thieblemont D, Triboulet C, Chevremont P (1994) Palaeogeographical reconstructions of the Pan-African/Brasiliano orogen: closure of an oceanic domain or intracontinental convergence between major blocks? Precambrian Res 67:327–344

da Silva Filho AF, Guimarães IP, Thompson RN (1993) Shoshonitc and ultrapotassic Proterozoic intrusive suites in the Cachoeirinha-Salgueiro Belt, NE Brazil: a transition from collisional to postcollisional magmatism. Precambrian Res 62:323–342

Dawaï D, Bouchez J-L, Paquette J-L, Tchameni R (2013) The Pan-African quartz-syenite of Guider (north-Cameroon): magnetic fabric and U–Pb dating of a late-orogenic emplacement. Precambrian Res 236:132–144

De Witt M, Stankiewicz J, Reeves C (2008) Restoring Pan-African-Brasiliano connections: more Gondwana control, less Trans-Atlantic corruption. Geol Soc Lond Spec Publ 294:399–412. doi:10.1144/SP294.20

Dumont JF, Toteu F, Penaye J (1985) Ensembles structuraux et principales phases de déformation panafricaines dans la zone mobile du Nord Cameroun, Région de Poli. Revue des Sciences et Techniques. Série Sciences de la Terre. Yaoundé 1:9–23

Enami M, Suzuki K, Liou JG, Bird DK (1993) Al–Fe^{3+} and F-OH substitutions in titanite and constraints on their P-T dependence. Eur J Mineral 5:219–231

Evans BW, Vance JA (1987) Epidote phenocrysts in dacitic dikes, Boulder County, Colorado. Contrib Mineral Petrol 96:178–185

Farrow CEG, Barr SM (1992) Petrology of high-Al-hornblende and magmatic epidote-bearing plutons in the southeastern Cape Breton Highlands, Nova Scotia. Can Mineral 30:377–392

Ferreira VP, Sial AN (1997) Two distinct sources for ultrapotassic magmas in the Transverse Zone, northeastern Brazil: oxygen and Nd isotopes. Semana de Geoquímica, 10, Congresso de Geoquimica dos Países de Lingua Portuguesa, 4, Braga, 1997, Actas, Braga, 43

Ferreira VP, Sial AN, Pimentel MM, Moura CAV (2004) Intermediate to acid magmatism and crustal evolution in the Transversal Zone, Northeastern Brazil. Geologia de Continente Sul-Americano: Evolução da obra de Fernando Flávio de Almeida, pp 190–201

Ferreira VP, Sial AN, Pimentel MM, Armstrong R, Spicuzza M, Guimarães I, Silva Filho AF (2011) Contrasting sources and P-T crystallization conditions of epidote bearing granitic rocks, Northeastern Brazil: O, Sr and Nd isotopes. Lithos 121:189–201

Galindo AC, Dall'Agnol R, Lafon JM, Teixeira NP (1995) Evolution of Brasiliano-age granitoid types in a shear-zone environment, Umarizal-Caraubas region, Rio Grande do Norte, northeast Brazil. J S Am Earth Sci 8:79–95

Green TH, Watson EB (1982) Crystallization of apatite in natural magmas orogenic rock series. Contrib Mineral Petrol 79:96–105

Guimaraes IP, Silva Filho AF, Almeida CN, Van Schmus WR, Araŭjo JMM, Melo SC, Melo EB (2004) Brasiliano (Pan-African) granitic magmatism in the Pajeŭ-Paraĭba belt, Northeast Brazil: an isotopic and geochronological approach. Precambrian Res 135:23–53

Hammarstrom JM, Zen E-A (1983) Possible use of Al content in hornblende as geobarometer for plutonic rocks. In: Geological Society of America, Annual Meeting, Abstracts with Programs, vol 590. Indianapolis

Hammarstrom JM, Zen E (1986) Aluminum in hornblende: an empirical igneous geobarometer. Am Mineral 71:1297–1313

Holdaway MJ (1972) Thermal stability of Al–Fe epidotes as a function of fO_2 and Fe contents. Contrib Mineral Petrol 37:307–340

Holland T, Blundy J (1994) Non-ideal interactions in calcic amphiboles and their bearing on amphibole-plagioclase thermometry. Contrib Mineral Petrol 116:433–447

Hollister LS, Ge Grissom, Peters EK, Stowell HH, Sisson VR (1987) Confirmation of the empirical correlation of AI in hornblende with pressure of solidification of calc-alkaline plutons. Am Mineral 72:231–239

Isseini M, André-Mayer AS, Vanderhaeghe O, Barbey P, Deloule E (2012) A-type granites from the Pan-African orogenic belt in south-western Chad constrained using geochemistry, Sr–Nd isotopes and U–Pb geochronology. Lithos 153:39–52

Johnson MC, Rutherford MJ (1989) Experimental calibration of the aluminum in-hornblende geobarometer with application to Long Valley caldera (California) volcanic rocks. Geology 17:837–841

Johnston AD, Wyllie PJ (1988) Constraints on the origin of Archean trondhjemites based on phase relationships of Nuk gneiss with H_2O at 15 kbar. Contrib Mineral Petrol 100:35–46

Kwékam M, Affaton P, Bruguier O, Liégeois J-P, Hartmann G, Njonfang E (2013) The Pan-African Kekem gabbro-norite (West-Cameroon), U–Pb zircon age, geochemistry and Sr–Nd isotopes: Geodynamical implication for the evolution of the Central African fold belt. J Afr Earth Sci 84:70–88

Lasserre M (1967) Données géochronologiques nouvelles acquises au 1er janvier 1967 par la méthode au strontium appliquée aux formations cristallines et cristallophylliennes au Cameroun. Ann Fac Sci Univ Clermont-Ferrand Géol Minéral 36:109–144

Leake BE, Wooley AR, Arps CES, Birch WDE, Gilbert MC, Grice JD, Hawthorne FC, Kato A, Kisch HJ, Krivovichev VG, Linthout K, Laird J, Mandarino JA, Maresch WV, Nickel EH, Rock NMS, Schumacher JC, Smith DC, Stephenson L, Ungaretti L, Whittaaker EJW, Youzhi G (1997) Nomenclature of amphiboles: report of the subcommittee on amphiboles of the International Mineralogical Association, Commission on New Minerals and Mineral Names. Am Mineral 82:1019–1037

Liégeois J-P, Abdelsalam MG, Ennih N, Ouabadi A (2013) Metacraton: nature, genesis and behavior. Gondwana Res 23:220–237

Liu YS, Hu ZC, Zong KQ, Gao CG, Gao S, Xu J, Chen HH (2010) Reappraisement and refinement of zircon U–Pb isotope and trace element analyses by LA-ICP-MS. Chin Sci Bull 55:1535–1546

Long LE, Castellana HC, Sial AN (2005) Age, origin and cooling history of the Coronel João pluton, Bahia, northeastern Brazil. J Petrol 46(2):255–273

Ludwig KR (1998) On the treatment of concordant uranium–lead ages. Geochim Cosmochim Acta 62(4):665–676

Ludwig KR (2003) User's Manual for Isoplot 3.0: A geochronological Toolkit for Microsoft Excel, vol 4. Berkeley Geochron Center, Berkeley, pp 1–71

Mason GH (1985) The mineralogy and textures of the Coastal Batholith, Peru. In: Pitcher WS, Atherton MP, Cobbing EJ, Beckinsale RD (eds) Magmatism at a plate edge: the Peruvian Andes. Blackie Halstead Press, Glasgow, pp 156–166

Naney MT (1983) Phase equilibria of rock-forming ferromagnesian silicates in granitic systems. Am J Sci 283:993–1033

Neves SP, Monié P, Bruguier O, da Silva JMR (2012) Geochronological, thermochronological and thermobarometric constraints on deformation, magmatism and thermal regimes in eastern Borborema Province (NE Brazil). J S Am Earth Sci 38:129–146

Ngako V, Njonfang E (2011) Plates amalgamation and plate destruction, the Western Gondwana history. In: Closson Damien (ed) Tectonics. INTECH, UK, p 358

Ngako V, Affaton P, Nnange JM, Njanko T (2003) Pan-African tectonic evolution in central and southern Cameroon: transpression and transtension during sinistral shear movements. J Afr Earth Sci 36:207–214

Ngako V, Affaton P, Njonfang E (2008) Pan-African tectonics in northwestern Cameroon: implications for the history of western Gondwana. Int Assoc Gondwana Res 14:509–522

Nzenti JP, Ngako V, Kambou R, Penaye J, Bassahak J, Njell OU (1992) Structures régionales de la chaîne panafricaine du Nord Cameroun. Comptes Rendus Académie des Sciences Paris, série II 315:209–215

Oliveira EP, Toteu SF, Araujo MNC, Carvalho MJ, Nascimento RS, Bueno JF, Mc Naughton N, Basilici G (2006) Geologic correlation between the Neoproterozoic Sergipano belt (NE Brazil) and the Yaounde Belt (Cameroon, Africa). J Afr Earth Sci 44:470–478

Owen JV (1991) Significance of epidote in orbicular diorite from the Grenville Front Zone, eastern Labrador. Mineral Mag 55:173–181

Pearce JA, Harris NBW, Tiindle AG (1984) Trace element discrimination diagrams for the tectonic interpretation of granitic rocks. J Petrol 25:956–983

Penaye J, Toteu SF, Tchameni R, Van Schmus WR, Tchakounté J, Ganwa A, Minyem D, Nsifa EN (2004) The 2.1 Ga West Central African belt in Cameroon. J Afr Earth Sci 39:159–164

Penaye J, Kröner A, Toteu SF, Van Schmus WR, Doumnang JC (2006) Evolution of the Mayo Kebbi region as revealed by zircon dating: an early (ca. 740 Ma) Pan-African magmatic arc in southwestern Chad. J Afr Earth Sci 44:530–542

Rogers JJW (1988) The Arsikere Granite of southern India: magmatism and metamorphism in a previously depleted crust. Chem Geol 67:155–163

Schmidt MW (1992) Amphibole composition in tonalite as a function of pressure: an experimental calibration of the Al-in-hornblende-barometer. Contrib Mineral Petrol 110:304–310

Schmidt MW, Thompson AB (1996) Epidote in calc-alkalic magmas: an experimental study of stability phase relationships, and the role of epidote in magmatic evolution. Am Mineral 81:462–474

Shand SJ (1927) Eruptive rocks. Their genesis, composition, classification, and their Relation to ore-deposits, 3rd edn. Wiley, New York, p 488

Sial AN (1986) Granite-types in Northeast Brazil: current knowledge. Rev Brasil Geosci 16:54–72

Sial AN (1993) Contrasting metaluminous magmatic epidote-bearing granitic suites from two Precambrian Foldbelts in Northeast Brazil. An Acad Bras Cienc 65(suppl 1):141–162

Sial AN, Toselli AJ, Saavedra J, Ferreira VP (1999) Emplacement, petrological and magnetic susceptibility characteristics of diverse magmatic epidote-bearing granitoid rock in Brazil, Argentina and Chile. Lithos 46:367–392

Sial AN, Vasconcelos PM, Ferreira VP, Pessoa RR, Brasilino RG, Morais Neto JM (2008) Geochronological and mineralogical constraints on depth of emplacement and ascension rates of epidote-bearing magmas from northeastern Brazil. Lithos 105:225–238

Streckeisen A, Le Maitre RW (1979) A chemical approximation to the modal QAPF classification of the igneous rocks. Neues Jahrbuch fuer Mineralogie Abhandlung 136:169–206

Sun S-S, McDonough WF (1989) Chemical and isotopic systematics of oceanic basalts: implications for mantle composition and processes. In: Saunders AD, Norry MJ (eds) Magmatism in the ocean basins, vol 42. Geological Society of London Special Publication, pp 313–345

Toteu SF, Van Schmus RW, Penaye J, Michard A (2001) New U–Pb and Sm–Nd data from North-Central Cameroon and its bearing on the pre-Pan-African history of central Africa. Precambrian Res 108:45–73

Toteu SF, Penaye J, Poudjom Djomani Y (2004) Geodynamic evolution of the Pan-African belt in central Africa with special reference to Cameroon. Can J Earth Sci 41:73–85

Toteu SF, Penaye J, Deloule E, Van Schmus WR, Tchameni R (2006) Diachronous evolution of volcano-sedimentary basins north of the Congo craton: insights from U–Pb ion microprobe dating of zircons from the Poli, Lom and Yaounde Series (Cameroon). J Afr Earth Sci 44:428–442

Trompette R (1997) Neoproterozoic (~600 Ma) aggregation of Western Gondwana: a tentative scenario. Precambrian Res 82:101–112

Tulloch AJ (1979) Secondary Ca-Al silicates as low-grade alteration products of granitoid biotite. Contrib Mineral Petrol 69:105–117

Tulloch AJ (1986) Comments and Reply on "Implications of magmatic epidote-bearing plutons on crustal evolution in the accreted terranes of northwestern North America" and "Magmatic epidote and its petrologic significance". Geology 14:186–187

Van Schmus WR, Oliveira EP, Da Silva Filho AF, Toteu SF, Penaye J, Guimães IP (2008) Proterozoic links between the Borborema Province, NE Brazil, and the Central African Fold Belt. J Geol Soc (Lond) 294:69–99

Vlach SRF, Gualda GAR (2007) Allanite and chevkinite in A-type granites and syenites of the Graciosa Province, southern Brazil. Lithos 97:98–121

Vyhnal CR, McSween HY Jr, Speer JA (1991) Hornblende chemistry in southern Appalachian granitoids: implications for aluminum hornblende thermobarometry and magmatic epidote stability. Am Mineral 76:176–188

Watson EB (1987) The hole of accessory minerals in granitoid geochemistry. In: Hutton Conference of the Origin of Granites: Transactions of the Royal Society of Edinburgh, pp 209–211

Watson EB, Harrison MT (1984) Zircon saturation revisited: temperatures and composition effects in a variety of crustal magma types. Earth Plan Sci Lett 104:381–397

Wones DR (1989) Significance of the assemblage titanite + magnetite + quartz in granitic rocks. Am Mineral 74:744–749

Yuan HL, Gao S, Liu XM, Li HM, Gunther D, Wu FY (2004) Accurate U–Pb age and trace element determinations of zircon by laser ablation-inductively coupled plasma mass spectrometry. Geostand Newsl 28:353–370

Zen E-A (1988) Tectonic significance of high pressure plutonic rocks in the Western Cordillera of North America. In: Ernst WG (ed) Metamorphism and Crustal Evolution of the Western United States, Rube, vol VIII. Prentice-Hall, Engelwood Cliffs, New Jersey, pp 41–71

Zen E, Hammarstrom JM (1984) Magmatic epidote and its petrologic significance. Geology 12:515–518